ANNUAL REVIEWS

Annual Review of Physical Chemistry

Photophysics of Two-Dimensional Semiconducting Organic–Inorganic Metal-Halide Perovskites

Daniel B. Straus[1] and Cherie R. Kagan[2]

[1]Department of Chemistry, Princeton University, Princeton, New Jersey, USA

[2]Department of Electrical and Systems Engineering, Department of Materials Science and Engineering, and Department of Chemistry, University of Pennsylvania, Philadelphia, Pennsylvania, USA; email: kagan@seas.upenn.edu

Annu. Rev. Phys. Chem. 2022. 73:403–28

First published as a Review in Advance on February 4, 2022

The *Annual Review of Physical Chemistry* is online at physchem.annualreviews.org

https://doi.org/10.1146/annurev-physchem-082820-015402

Keywords

hybrid perovskite, excitons, phonons, spectroscopy, dynamics

Abstract

Two-dimensional organic–inorganic hybrid perovskites (2DHPs) consist of alternating anionic metal-halide and cationic organic layers. They have widely tunable structural and optical properties. We review the role of the organic cation in defining the structural and optical properties of 2DHPs through the example of lead iodide 2DHPs. Even though excitons reside in the metal-halide layers, the organic and inorganic frameworks cannot be separated—they must be considered as a single unit to fully understand the photophysics of 2DHPs. We correlate cation-induced distortion and disorder in the inorganic lattice with the resulting optical properties. We also discuss the role of the cation in creating and altering the discrete excitonic structure that appears at cryogenic temperatures in some 2DHPs, including the cation-dependent presence of hot-exciton photoluminescence. We conclude our review with an outlook for 2DHPs, highlighting existing gaps in fundamental knowledge as well as potential future applications.

1. INTRODUCTION

Semiconductors have an electronic structure that can be considered to be just right, with band gaps tailorable through the optical spectrum by composition and dimension, and carrier concentrations that can be modulated by external stimuli (1). The properties of semiconductors are of fundamental scientific interest in order to understand matter and its interactions, particularly with light and voltage (2). They are also harnessed in electrical and optoelectronic devices for applications in sensing, energy, computation, and communications technologies (3). Conventional semiconductors are extended inorganic materials, namely elemental group IV semiconductors; compound III–V, II–VI, and IV–VI semiconductors; and ternary and quaternary semiconductors. In addition, they may be bulk solids or low-dimensional homo- or heterostructures. Organic materials such as aromatic molecular crystals as well as oligomeric and polymeric solids may also be semiconducting (4). Finally, organic–inorganic hybrid materials also form semiconductors. They combine the properties of organic and inorganic materials, greatly increasing their complexity both in the number of possible compositions and in their physical properties. These materials include assemblies of colloidal nanostructures (5, 6) as well as metal-halide hybrid perovskites (7, 8), which are the focus of this review.

Inorganic metal-halide perovskites are stoichiometric compounds with the chemical formula AMX_3 (9–12) (**Figure 1*a***). A singly charged cation (A^+) occupies the interstitial space in a corner-sharing network of MX_6 octahedra, with M being a 2+ metal (typically Pb^{2+} or Sn^{2+}) and X a halide (Cl^-, Br^-, or I^-). The size of the A-site cation is limited by the available volume of the interstitial space between the MX_6 octahedra—if A^+ is too small or too large, a three-dimensional (3D) perovskite cannot form. This principle is formalized through the Goldschmidt tolerance factor (13, 14), which is derived from the principle that an ionic structure is stable when the number of cation–anion contacts is maximized and free volume within a structure is minimized (15). Based on the available volume in the voids between the MX_6 octahedra, the only inorganic cation that forms a stable perovskite structure with Pb^{2+} or Sn^{2+} is Cs^+, the largest 1^+ inorganic cation (16). Even Cs^+ is too small for $CsPbI_3$ to be a stable perovskite (17).

Organic–inorganic hybrid perovskites replace the A^+ inorganic cation with a positively charged organic molecule, greatly increasing the phase space of possible materials (7). In a 3D

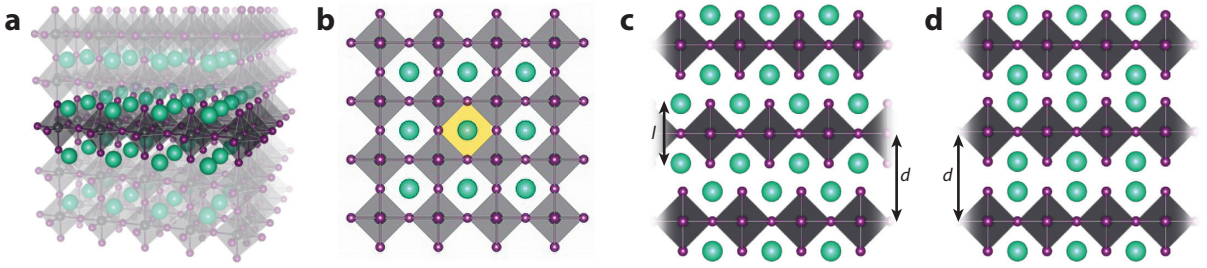

Figure 1

Constructing two-dimensional organic–inorganic hybrid perovskites (2DHPs). (*a*) Cubic three-dimensional (3D) halide perovskite with the formula AMX_3, with A^+ as green, M^{2+} as gray, and X^- as purple spheres. MX_6 octahedra are shaded in gray. 2DHPs are constructed by taking a single A_2MX_4 layer (*darker atoms*) from the overall 3D structure. (*b*) Top view of a single layer of a 2DHP, with the maximum cross-sectional area highlighted in yellow. Different stacking arrangements are possible in 2DHPs. (*c*) The Ruddlesden-Popper phase, in which each layer is offset from another by half a lattice constant, and (*d*) the Dion-Jacobson phase, in which there is no offset between layers in at least one direction. The interlayer spacing *d* is the distance between planes of Pb atoms in adjacent inorganic layers (*black arrows*), and the thickness of the inorganic layer *l* is the distance between axial X atoms in an octahedron.

hybrid perovskite (3DHP), the organic cation must be small, and the most popular choice is methylammonium ($CH_3NH_3^+$). First discovered in 1978 (18, 19), hybrid perovskites attracted tremendous attention starting in the mid-2000s, when they were first used for solar energy conversion (20, 21). The efficiency of hybrid perovskite solar cells has rapidly increased and now rivals that of commercial silicon-based solar cells (22).

While increasing the total size of the cation prevents the perovskite structure from forming, increasing the length of the cation results in the spontaneous formation of two-dimensional (2D) hybrid perovskites (2DHPs) (23). A typical 2DHP can be constructed by cutting a single layer of corner-sharing octahedra out of a 3D perovskite, including the cations on both sides (**Figure 1*a***), and then stacking these layers on top of each other. This results in a material with the formula A_2MX_4. A top-down view of a single layer of a 2DHP is shown in **Figure 1*b***. A_2MX_4 2DHPs are van der Waals materials, and the stacking of 2DHP layers in thin films or crystal(lites) can occur in multiple ways (24–26). If the individual layers are offset from one another by half a lattice constant in both directions, they are referred to as Ruddlesden-Popper phase (**Figure 1*c***). Conversely, if there is no offset in one or both directions, the Dion-Jacobson phase occurs (**Figure 1*d***). Both Ruddlesden-Popper and Dion-Jacobson 2DHPs have been synthesized (25). While a cation with too large a cross-sectional area (see **Figure 1*b***) disrupts 2DHP formation, there are no known restrictions on the length of the cation (7). The flexibility in the choice of cation provides tremendous structural diversity in 2DHPs (24, 25), with the ability to tune the structure by the choice of cation within the limit of the cross-sectional area of the cation.

This review limits its consideration to monolayer 2DHPs, in which the inorganic framework is a single layer of the parent 3DHP material (**Figure 1*a***) and the shared corners of the octahedra are all located on a single plane (**Figure 1*c*,*d***). We do not discuss examples with alternate octahedral connectivity or thicker inorganic frameworks [that is, with multiple (two or more) inorganic layers per organic cationic layer] (7). We also limit our consideration to 2DHPs in which the states that originate from the A-site cations are far from the edges of the metal-halide valence and conduction bands. 2DHPs with this electronic structure confine carriers and excitons to the inorganic framework. This electronic structure is known as a Type I band alignment, which is also seen in semiconductor quantum well superlattices (24, 27). The most-studied inorganic framework is composed of <100> Pb–I inorganic layers, which we focus on in this review to exemplify the photophysics of 2DHPs.

Common to the study of all semiconductors is the importance of optical spectroscopy, a key tool of physical chemists, in studying the electronic and vibrational structure and the dynamics of excitons, electrons, and phonons in semiconductors (2, 4, 28). In this review, we highlight how the optical properties of excitons in 2DHPs can be tuned through the choice of cation without varying the metal or halide. We review several situations in which the organic cation is required to understand and model the properties of excitons in 2DHPs and explore how changes in the composition, length, and cross-sectional area of the cation influence the photophysical properties of excitons. Section 2 discusses the electronic structure of 2DHPs, examining the impact of quantum and dielectric confinement effects on the 2DHP semiconductor band structure and on the energy of excitons. Section 3 illustrates the impact of cation-induced structural changes on the optical and electronic properties of 2DHPs. In Section 4, we examine how longer cations impact the energy landscape of 2DHPs. Section 5 considers the origin of the low-temperature structure in the excitonic absorption and photoluminescence resonances, focusing on the hypothesis that the organic cation is responsible for this structure. Lastly, Section 6 gives an outlook on future directions in the study of 2DHPs.

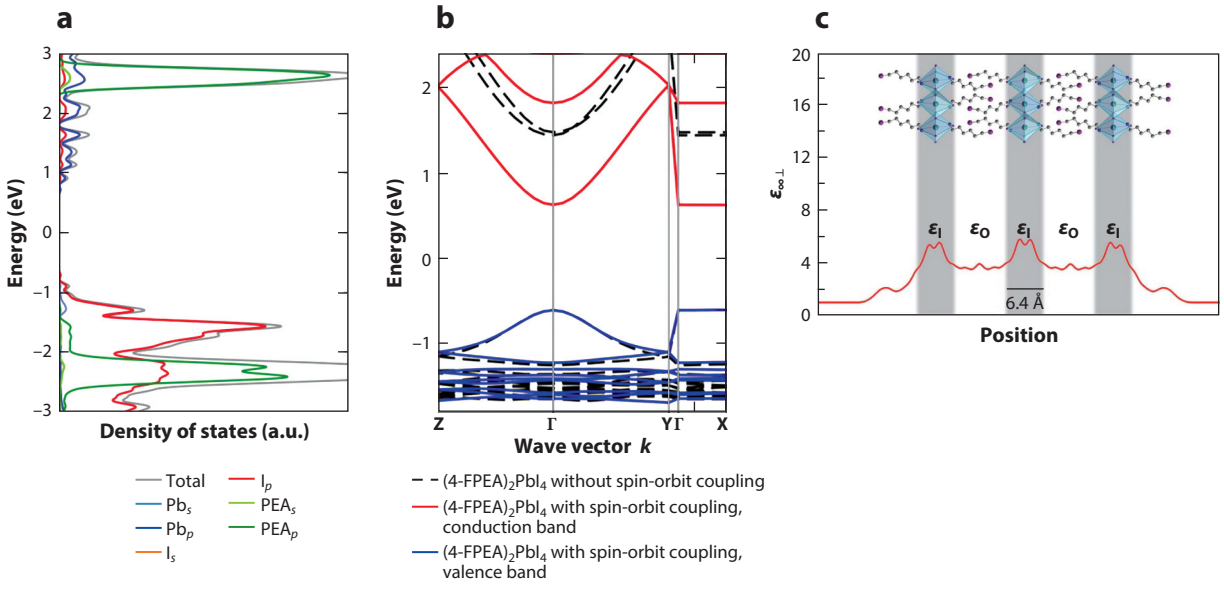

Figure 2

Electronic structure. (*a*) Density of states for $(PEA)_2PbI_4$. Panel *a* adapted with permission from Reference 32; copyright 2017 American Chemical Society. (*b*) Band structure for $(4\text{-FPEA})_2PbI_4$ without (*dashed black lines*) and with (*solid blue and red lines*) spin-orbit coupling. Panel *b* adapted with permission from Reference 35; copyright 2016 American Chemical Society. Γ, X, Y, and Z are high symmetry points in reciprocal (*k*) space. (*c*) Dielectric profile perpendicular to PB–I layers of $(IC_6H_{12}NH_3)2PbI_4$. $\varepsilon_{\infty\perp}$ is the high-frequency dielectric constant in the direction perpendicular to the inorganic layers. ε_I and ε_O are the dielectric constants of the inorganic and organic frameworks, respectively. Panel *c* adapted with permission from Reference 36; copyright 2017 Royal Society of Chemistry. Abbreviation: PEA, phenethylammonium ($C_6H_5C_2H_4NH_3^+$).

2. MODELING THE PROPERTIES OF 2DHPS

2.1. Band Structure

The band structure in solid-state theory describes the dispersion relationship between the energy and wave vector (*k*) of an electron (29). Conventional semiconductors have a valence band derived from atomic *p*-orbitals and a conduction band derived from atomic *s*-orbitals yielding more complex, near-degenerate heavy and light holes as well as spin-orbit, split-off valence bands but only a single conduction band (3, 30). In contrast, metal-halide perovskites have a band structure different from that of conventional semiconductors. The valence band of halide perovskites is composed of antibonding orbitals formed from halide *p*-orbitals and metal *s*-orbitals, while the conduction band is predominantly derived from antibonding orbitals composed of metal *p*-orbitals (31, 32) (**Figure 2*a***). This band structure leads to one valence band but complexity in the conduction band, including significant spin-orbit coupling effects that are especially important for structures containing heavy atoms such as Pb and Sn (**Figure 2*b***) (33). This is true in both 3D and 2DHPs for the most commonly studied aliphatic or short aromatic (e.g., phenyl or naphthyl) ammonium A-site cations (34), in which states originating with the A-site cation are far from the metal-halide band edges. The 2DHPs therefore have a Type I band alignment. Thus, in 2DHPs, the inorganic and organic sublattices are commonly considered separately (31, 34). Under this simple model, the composition of the metal and halide of the inorganic sublattice defines the conduction and valence band energies, and the organic sublattice acts solely as an insulating spacer between the inorganic metal-halide layers. At this level of theory, 2DHPs are functionally equivalent to semiconductor

quantum well superlattices prepared by molecular beam epitaxy, with the advantage that 2DHPs are free from interfacial roughness (24, 27).

In 2DHPs, the inorganic framework extends infinitely in two directions, but the thickness l of the inorganic framework (**Figure 1*c*,*d***) is restricted. For example, the thickness of a layer in lead iodide 2DHPs is only ∼6.3 Å (37). While the band structures of 3D and 2DHPs have the same atomic orbital contributions and are thus similar, in 2DHPs, strong quantum confinement effects are present in one dimension, which increases their band gap compared to that of similar 3DHPs (38). Assuming the organic framework imposes an infinite confinement potential, the energy of the valence (conduction) band of the 2DHP decreases (increases) by $\frac{\hbar^2\pi^2}{2m_{e,h}l^2}$ compared to a similar 3D perovskite, where l is the thickness of the inorganic framework and $m_{e,h}$ is the mass of the hole (electron) (31).

The layered structure also gives rise to dielectric contrast between the high dielectric constant inorganic framework ε_I and the lower dielectric contrast layer of organic cations ε_O (**Figure 2*c***). This contrast gives rise to dielectric confinement effects. Because the inorganic layers are thin compared to the Bohr exciton radius (39), the electric field generated by a charge carrier located in the inorganic framework extends into the organic framework, where the screening of the field is weaker (40, 41). The reduction in dielectric screening increases the Coulomb potential in the inorganic layers, in turn increasing the band gap (42).

2.2. Excitons

In 3D perovskites, the excitonic resonance is not well-separated from the band-edge absorption at room temperature. 3D lead iodide perovskites such as methylammonium lead iodide ($CH_3NH_3PbI_3$) and cesium lead iodide ($CsPbI_3$) have reported binding energies of 12 to 16 meV and 18 meV, respectively (43, 44), so at room temperature ($kT = 26$ meV), all excitons spontaneously separate into free electrons and holes. In contrast, Type I 2DHPs have a sharp excitonic absorption resonance that is well-separated from the onset of the continuum absorption (38) (**Figure 3*a***). Minimal electronic coupling between adjacent inorganic layers is found in most 2DHPs (45). Quantum and dielectric confinement greatly increase the exciton binding energy in 2DHPs by over an order of magnitude compared to their parent 3D materials, resulting in exciton binding energies that typically exceed 150 meV.

In a perfect quantum well that is infinitely thin and has an infinite confinement potential, quantum confinement effects increase the binding energy such that $E_b = 4E_0$, where $E_0 = (\frac{1}{\varepsilon_I})^2(\frac{m_{ex}}{m_0})R_H$ is the exciton binding energy of the parent bulk 3D material, ε_I is the dielectric constant of the inorganic framework, $m_{ex} = (1/m_e + 1/m_b)^{-1}$ is the reduced mass of the exciton, m_0 the mass of an electron, and R_H the hydrogen Rydberg constant (48). Because the inorganic layers in 2DHPs are not infinitely thin and the confinement potential is finite, this serves as an upper bound on the true quantum confinement–induced exciton binding–energy enhancement. Quantum confinement would account for ∼60 meV of the 2DHP exciton binding energy based on the ∼15 meV binding energy in lead iodide 3DHPs (43, 44). Thus, quantum confinement alone cannot explain the enhancement in exciton binding energy.

Dielectric confinement effects account for the rest of the enhancement in 2DHP's exciton binding energy compared to 3DHPs. The Coulomb potential that binds the electron and hole together as an exciton is greatly increased by dielectric confinement, because the effective dielectric constant is smaller than that of the inorganic framework. The approximate increase in the exciton binding energy established by dielectric confinement is

$$\Delta E_b = 2\frac{\varepsilon_I - \varepsilon_O}{\varepsilon_I + \varepsilon_O}\frac{e^2}{\varepsilon_I l}A, \qquad 1.$$

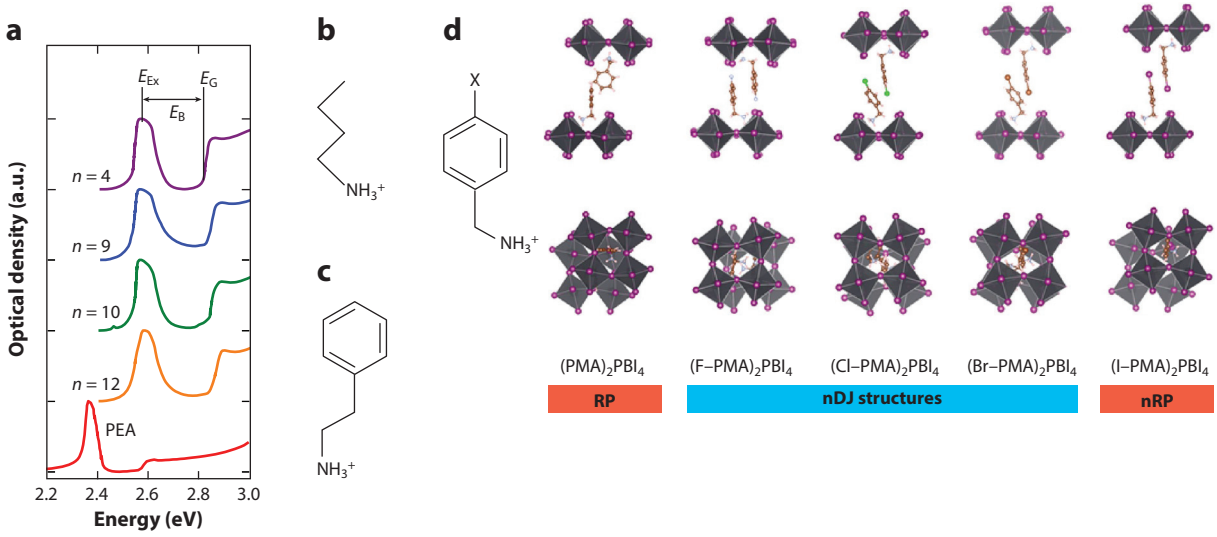

Figure 3

Quantum and dielectric confinement effects. (*a*) Absorption spectra of $(C_nH_{2n+1}NH_3)_2PbI_4$, taken at 1.6 K, and of $(PEA)_2PbI_4$, taken at 10 K, with the exciton energy E_{Ex}, band gap E_G, and exciton binding energy E_B labeled. Data from References 46 and 47. (*b*) Structure of $C_4H_9NH_3^+$, a representative alkylammonium cation. (*c*) Structure of the PEA cation. (*d*) Derivatives of the PMA cation can be used to tune the stacking motif between 2DHP layers from RP to DJ. Panel *d* adapted with permission from Reference 26; copyright 2019 American Chemical Society. Abbreviations: 2DHP, 2D organic–inorganic hybrid perovskite; DJ, Dion-Jacobson; nDJ, near-Dion-Jacobson; PEA, phenethylammonium ($C_6H_5C_2H_4NH_3^+$); PMA, phenylmethylammonium ($C_6H_5CH_2NH_3^+$); RP, Ruddlesden-Popper; nRP, near-Ruddlesden-Popper.

where e is the fundamental charge, l is the thickness of the inorganic layer, and A is a factor that depends on l and is slightly less than unity; the full equation is given in Reference 48.

2.3. Nonidealities in Real 2DHPs

In conventional inorganic quantum well superlattices, the one-dimensional (1D) periodic potential established by the semiconductor layers is captured by the Kronig-Penney model using the constituent semiconductor effective masses and requiring continuity of the wave functions at their interfaces (49). This simple model is successful in, for example, superlattices that have chemically similar constituent semiconductors, coherent interfaces, and Bloch functions (capturing the periodic potential of the unit cell) of the bulk materials that are similar at high symmetry points, so that the potential variation can be described by slow varying envelope functions and the atomic-scale potentials can be ignored. However, this simplified approximation breaks down when the semiconductors in a superlattice have very different electronic properties and their interfaces become structurally and electronically complex, such as having differences in local symmetry and electronic mixing between states at different points of the Brillouin zone (31).

In 2DHPs, the organic and inorganic layers are chemically very different. While treating the organic and inorganic frameworks separately allows for an intuitive understanding of how changes to the composition and structure of 2DHPs affect their band structure and exciton behavior, this simple model is, not surprisingly, inaccurate, and atomic-scale detail is necessary to capture the effects of quantum confinement. Even et al. (31) showed that the electronic properties of 3DHPs cannot be used to model the inorganic framework in 2DHPs. Charge carriers in 2DHPs are located at k-points away from the zone center where the bands of bulk 3DHPs are not parabolic, and,

thus, the 3DHP effective masses (found from the band curvatures near the extrema) are not valid (31, 38, 50). Assuming the organic framework imposes an infinite confinement potential is also not appropriate, because it overestimates that potential. However, even imposing a finite confinement potential with a sharp transition between the organic and inorganic layers is not sufficient to accurately model quantum confinement effects in 2DHPs (31). The Coulomb interactions between the cationic organic and anionic inorganic layers and the atomic-scale detail of the interfaces need to be taken into account.

The quantum confinement potential has been quantitatively modeled by considering 2DHPs as composites that capture their ionic character (31). For the representative 2DHP $(C_{10}H_{21}NH_3)_2PbI_4$, the inorganic sublattice is modeled as Na_2PbI_4, where the two Na^+ cations compensate for the negative charge of the $(PbI_4)^{2-}$ framework. The organic sublattice is modeled as $C_{10}H_{21}CH_3$, with the terminal N replaced by C to maintain charge neutrality of the combined $(C_{10}H_{21}CH_3)Na_2PbI_4$ model system. This method is shown to provide a good description of the electronic states close to the band edges, which are largely located in the inorganic layers, for the commonly explored 2DHPs with weak interactions between inorganic layers. It also describes the consistency in the electronic structure and energy gap of 2DHPs with similar inorganic structures.

While modeling the 2DHP superlattice in this more complex way accounts for quantum confinement, it is still too simplistic to capture the dielectric modulation and, thus, the effects of dielectric confinement on the electronic structure and exciton binding energy. Like the confinement potential, the dielectric constant is also more complex and is not a simple step function in which it adopts a fixed value in the inorganic layer and another fixed value in the organic layer. Instead, it is a smoothly varying function (**Figure 2*c***), and care must be taken to model it accurately, especially in the presence of intercalants (Section 2.5) or cations that result in an anisotropic dielectric profile in which the parallel and perpendicular components of the dielectric function take on different values (36).

Models that consider the organic and inorganic frameworks separately also do not capture the strong influence of the organic cation on the static and dynamic structures of the inorganic framework. The size and shape of the organic cations influence the structure of the inorganic sublattice, which in turn changes the band structure and affects how excitons and carriers behave (Section 3) (51). The influence of dynamic effects can be understood intuitively by considering the ionic nature of the material and the electrostatic interactions between the organic and inorganic sublattices—any motion of the positively charged ammonium group alters the electrostatic potential in the inorganic framework. Even if we consider a high-energy vibrational mode of the 2DHP in which only the cation moves because vibrations involving the heavy Pb and I atoms are low in energy (52), the electric field created by the positively charged organic cation is modulated by this motion. These and other subtleties are addressed in Sections 3–5.

2.4. Experimental Manifestations of Quantum and Dielectric Confinement

The principles discussed in Sections 2.1–2.3 are immediately apparent in optical spectra of 2DHPs. The large binding energy of the exciton and, thus, the large separation of its absorption resonances from the band edge is a signature of the strong contributions of quantum and dielectric confinement in 2DHPs. For the commonly studied alkylammonium (**Figure 3*b***) lead iodides $(C_nH_{2n+1}NH_3)_2PbI_4$, as n increases from 4 to 12, the interlayer Pb–Pb distances (d in **Figure 1*c*,*d***) increase from 15.17 to 24.51 Å. The exciton binding energy E_B is 320 ± 30 meV, and the band gap E_G is ~2.88 eV at 1.6 K for all of these 2DHPs (47) (**Figure 3*a***). $(C_3H_7NH_3)_2PbI_4$ also forms a 2DHP with an interlayer Pb–Pb distance of 13.81 Å. Its optical properties do not differ

from those of $(C_4H_9NH_3)_2PbI_4$, but unlike the other alkylammonium 2DHPs, $(C_3H_7NH_3)_2PbI_4$ converts to a nonperovskite phase upon exposure to moisture (53). $C_2H_5NH_3^+$ does not form a 2DHP with Pb and I and, instead, forms 1D chains of face-sharing Pb–I octahedra (54), and $CH_3NH_3PbI_3$ is the prototypical 3DHP. All $(C_nH_{2n+1}NH_3)_2PbI_4$ 2DHPs therefore experience a similar degree of quantum confinement, and a minimum critical length for the presence of full quantum confinement effects in alkylammonium 2DHPs cannot be experimentally established. Note that because the optical properties do not change in these 2DHPs, the inorganic layers do not interact, or at most weakly interact, with one another (i.e., there are no superlattice effects) (31). 2DHPs with shorter cations have been synthesized (55), and theoretical studies on the 2DHP $(IC_2H_4NH_3)_2PbI_4$ indicate that it shows a reduced degree of quantum confinement compared to those of $(C_nH_{2n+1}NH_3)_2PbI_4$ 2DHPs. Unlike most 2DHPs, it is expected to exhibit weak superlattice effects (31, 45).

Dielectric confinement effects can be used to tune the exciton binding energy even if the degree of quantum confinement is invariant. As the difference between ε_I and ε_O decreases, the exciton binding energy decreases according to Equation 1. This can be seen in **Figure 3*a***—the conjugated phenethylammonium ($C_6H_5C_2H_4NH_3^+$, PEA; shown in **Figure 3*c***) cation has a larger dielectric constant than do unconjugated alkylammonium ($C_nH_{2n+1}NH_3^+$) cations, and, accordingly, $(PEA)_2PbI_4$ has a smaller exciton binding energy of 190–220 meV (46, 52). It also has a smaller band gap, though some of the change in band gap can be attributed to the presence of additional strain in the inorganic framework (Section 3).

Dielectric confinement effects can be exploited to tune the exciton binding energy in a single 2DHP without synthetically modifying the cation. Intercalating molecular I_2 in the organic framework of the 2DHP $(IC_6H_{12}NH_3)_2PbI_4$ increases ε_O. After the intercalation process, the band gap decreases by 70 meV from 2.56 to 2.49 eV, and the exciton binding energy decreases by 50 meV from 230 to 180 meV (36). The molecular I_2 can be deintercalated, returning the band gap and exciton binding energies to the original values for $(C_6H_{12}NH_3)_2PbI_4$. In addition, when a single layer of the 2DHP butylammonium lead iodide $[(C_4H_9NH_3)_2PbI_4]$ is exfoliated and placed on a silica ($\varepsilon = 2.13$) substrate with air ($\varepsilon = 1$) on top, the exciton binding energy E_B increases to 490 meV for the monolayer and from ~320 to 370 meV in the multilayer 2DHP (56).

The stacking motif can be varied by tuning intermolecular interactions between the cations (26, 57) (**Figure 3*d***) or by using more rigid bidentate cations (58), in which a single A^{2+} cation has a positively charged ammonium functional group at each end, for an overall formula of AMX_4. Because these cations are all longer than $C_3H_7NH_3^+$, there is no difference in the optical or electronic properties of the 2DHPs shown in **Figure 3*d*** that can be attributed to differences in the stacking motif (26). Subtle spectral changes may emerge at cryogenic temperatures from differences in stacking arrangement (58).

3. CATION-INDUCED CHANGES TO THE INORGANIC FRAMEWORK

Thus far, we have neglected to consider how changes to the structure of the inorganic framework also affect the optical properties of 2DHPs. The model perovskites in **Figure 1** exhibit no distortion—the PbI_6 octahedra have equal Pb–I bond lengths and 90° internal I–Pb–I bond angles. In addition, the octahedra are not tilted with respect to one another—the bridging Pb–I–Pb bond angles (θ in **Figure 4*a***) are 180°.

Real 2DHPs display some degree of distortion (**Figure 4*b***)—we are unaware of any experimental examples with completely undistorted cubic inorganic frameworks. The PbI_6 octahedra are tilted with respect to one another, and, accordingly, θ is less than 180°. Even in distorted 2DHPs, the inorganic layers are usually planar (**Figure 4*c***). However, in highly distorted 2DHPs,

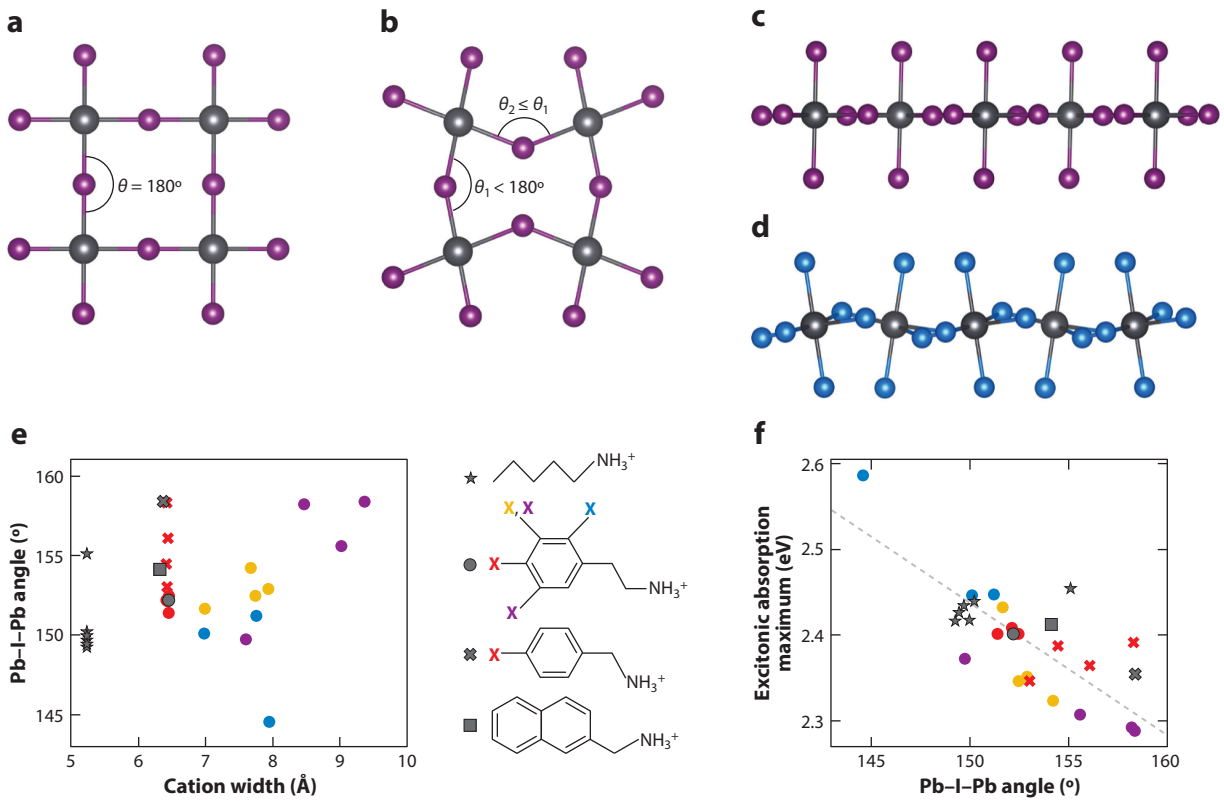

Figure 4

Distortion in the inorganic framework. (*a*) Top view of a perfect cubic 2D organic–inorganic hybrid perovskite (2DHP), with the Pb–I–Pb angle $\theta = 180°$. (*b*) Top view of a distorted 2DHP, in which $\theta_2 \leq \theta_1 < 180°$. (*c*) Planar and (*d*) corrugated inorganic frameworks. (*e*) Scatter plot of cation width and θ for experimental Pb–I 2DHPs, in which the symbol shape corresponds to the cation family and color is used to specify the type of substitution. (*f*) Scatter plot of room-temperature excitonic absorption maximum and Pb–I–Pb angle for experimental 2DHPs. Linear fit excluding $(C_nH_{2n+1}NH_3)_2PbI_4$ (*stars*) is shown in gray. Data in panels *e* and *f* from References 26, 37, and 59–64.

the inorganic framework buckles and the inorganic layers appear corrugated (**Figure 4*d***). This section discusses how the degree of distortion can be tuned through cation modification, as well as the effect of inorganic lattice distortions on the optical properties of 2DHPs.

3.1. Cation-Induced Structural Changes

A large library of cations can be used to synthesize 2DHPs, as there is only a restriction on the cation's cross-sectional area (25). We highlight how the length, width, and composition of the organic cation induces structural changes in the 2DHPs (26, 37, 59, 60, 65). We examine several families of cations and discuss how modifications to the cation affect the inorganic framework and emphasize that this is not an exhaustive list of lead iodide–based 2DHPs. We point the reader to Reference 25 for a comprehensive list of 2DHPs indexed in the Cambridge Structural Database. The width of the cation is quantified by measuring the distance in the reported crystal structure between atoms orthogonal to the alkylammonium tether and adding the appropriate van der Waals radii (66) of the terminal atoms. For example, we quantify the width of PEA cations and

its derivatives as the distance between the two *ortho* or the two *meta* substituents on the phenyl group. If the Pb–I framework is asymmetric such that there are two or more distinct Pb–I–Pb bond angles θ ($\theta_2 \neq \theta_1$ in **Figure 4*b***), we report the average θ.

Alkylammonium ($C_nH_{2n+1}NH_3^+$) cations behave as one would expect—as the length of the cation gets longer (i.e., n increases), there is no regular change to the degree of distortion present in the inorganic framework, because the width of the cation remains unchanged (**Figure 4*e***). The structural similarity is seen for $n = 4$, 5, 7, 8, and 9. Interestingly, $n = 6$ is the exception and is significantly less distorted, with a ~5°-greater Pb–I–Pb bond angle than alkylammonium 2DHPs with $n \neq 6$ (65). For $n \neq 6$, there is a sharp discontinuity in the temperature-dependent excitonic absorption spectra, in which the excitonic resonance abruptly red-shifts upon warming between 235 and 310 K; this discontinuity is absent for $n = 6$, even though there is still a structural phase transition at 258 K (47, 63, 65). Despite the difference in their optical behavior, these are all first-order phase transitions (63, 64).

2DHPs with derivatives of the PEA cation exhibit different behavior depending on the class of structural modification performed on the cation. The length of the PEA cation can be increased without affecting the width by replacing the 4-position hydrogen (*para* to the ethylammonium tether) with a larger atom or functional group, such as a halogen or methyl group (**Figure 4*e***). These modifications increase the spacing between inorganic layers but do not significantly alter the inorganic framework, which can be seen by their very similar Pb–I–Pb angles (37).

Replacing the 2-position hydrogen (*ortho* to the ethylammonium tether) on the PEA cation with a larger substituent results in wider cations (**Figure 4*e***), and the inorganic frameworks of these 2DHPs are more distorted than that of unmodified $(PEA)_2PbI_4$ (59). The trend is not fully linear with size, however, as the 2-ClPEA cation is wider than the 2-FPEA cation yet results in a less distorted inorganic framework. The 2-Br cation results in the most distorted inorganic framework included in the plot, with an average Pb–I–Pb angle of 144.55°, and unlike the other $(PEA)_2PbI_4$ derivatives that have planar inorganic frameworks (**Figure 4*c***), its inorganic framework is corrugated (**Figure 4*d***).

Wider cations do not always distort the inorganic framework, however, such as in the family of $(PEA)_2PbI_4$ derivatives in which the 3-position hydrogen (*meta* to the ethylammonium tether) is replaced with a halogen or methyl group. While $(3\text{-XPEA})_2PbI_4$ (X = F) is more distorted than unsubstituted $(PEA)_2PbI_4$ (62), the inorganic framework becomes progressively less distorted as the width of the cation is further increased (X = Cl, Br, or Me), and these three 2DHPs are less distorted than is unsubstituted $(PEA)_2PbI_4$ (60) (**Figure 4*e***). Replacing both the 3- and 5-position *meta* hydrogens on the PEA cation with F, Cl, Br, or Me (**Figure 4*e***) results in a similar trend, with $(3,5\text{-FPEA})_2PbI_4$ being more distorted than unsubstituted $(PEA)_2PbI_4$ and the others being less distorted (60).

Replacing the ethylammonium tether on the PEA cation with a methylammonium tether results in the phenylmethylammonium ($C_6H_5CH_2NH_3^+$; PMA) cation, and $(PMA)_2PbI_4$ (**Figure 4*e***) is significantly less distorted than is $(PEA)_2PbI_4$ (61). Replacing the 4-position (*para*) hydrogen on the PMA cation with a larger atom or functional group (**Figure 4*e***) results in a very different trend than that observed with 4-XPEA cations. $(4\text{-FPMA})_2PbI_4$ displays a similar degree of distortion to unsubstituted $(PMA)_2PbI_4$, but $(4\text{-XPMA})_2PbI_4$ (X = Cl, Br, or I) are significantly more distorted, likely because of halogen-bonding interactions between the halogen on the cation and the axial I atoms in the inorganic framework (26). Ruddlesden-Popper and Dion-Jacobson perovskites are both found in this family of 2DHPs (**Figure 3*d***), and the stacking motif is tuned by halogen-bonding interactions between cations in adjacent layers (26).

We hypothesize that the differences in the degree of distortion between $(4\text{-XPEA})_2PbI_4$ and $(4\text{-XPMA})_2PbI_4$ 2DHPs originate from the methylammonium tether on the PMA cation being

less flexible than the ethylammonium tether on the PEA cation. While the longer ethylammonium tether in 4-XPEA cations allows the lattice to accommodate the longer substituted phenyl moieties, longer phenyl moieties in and/or halogen-bonding interactions between the 4-XPMA cations impose additional stress on the shorter methylammonium tether. This hypothesis is supported by the existence of the 2DHP 2-naphthylethylammonium lead iodide, in which the phenyl group in the PEA cation is replaced by the longer naphthyl group (**Figure 4*e***) (67). Despite the size of the cation, 2-naphthylethylammonium lead iodide is less distorted than is $(PEA)_2PbI_4$. However, the perovskite structure does not form if the 2-naphthylmethylammonium cation, which has a shorter alkylammonium tether, is used. Instead, an alternate type of structure forms that contains 1D chains of face-sharing lead iodide octahedra (61).

2DHPs have also been synthesized with chiral cations (68). Some chiral 2DHPs are optically active, in that they preferentially absorb and emit either left- or right-hand circularly polarized light (69–73).

3.2. Effect of Distortion on Optical Properties

The degree of distortion in the inorganic framework of a 2DHP directly affects its optical properties (51, 59, 67). We only consider the excitonic and continuum optical properties in this review and do not discuss the broad lower-energy photoluminescence resonance responsible for white light emission that is present in many 2DHPs. We suggest References 74–77 for theoretical and experimental analysis of this emission feature.

As the inorganic framework of the 2DHP becomes more distorted, the band gap increases. **Figure 4*f*** plots the energy of the room-temperature excitonic absorption maximum against the Pb–I–Pb bond angle for the same 2DHPs included in **Figure 4*e***. Because of the difficulty in determining the optical band gap at room temperature, we use the excitonic absorption maximum as a proxy. This is a valid approximation for cations with similar dielectric constants, because the exciton binding energies are similar (Sections 2.3 and 2.5). **Figure 4*f*** shows the result of a linear regression performed on the data points corresponding to 2DHPs with arylammonium cations, excluding those with alkylammonium cations. There is a strong correlation between the excitonic absorption maximum and the degree of distortion ($R^2 = 0.61$) that is highly statistically significant ($p = 1.6 \times 10^{-5} \ll 0.05$).

Knutson et al. (51) analyzed the changes in orbital overlap for Sn–I 2DHPs, and the same arguments apply for Pb–I 2DHPs. Increasing the Pb–I–Pb angle decreases the degree of orbital overlap between the metal *s*-orbitals and halide *p*-orbitals, lowering the energy of the top of the valence band. While a similar effect would also lower the top of the conduction band, the distortions break the symmetry of a perfect perovskite lattice and increase the antibonding interaction between metal *p*-orbitals and halogen orbitals. This increases the energy of the conduction band and therefore contributes to the widening of the band gap.

3.3. Effect of Temperature on Distortions and Optical Properties

While increasing the degree of distortion in the inorganic lattice directly correlates with a widening band gap, a more complicated picture emerges when considering temperature-dependent changes. **Figure 5** shows the temperature-dependent structural and optical properties of $(PEA)_2PbI_4$. Structural data is determined by single-crystal X-ray diffraction measurements. The 100 K and 300 K structures were previously reported in Reference 37 and are available at the Cambridge Crystallographic Data Centre under deposition codes 1977184 and 1977183, and the 125–275 K structures are available at the Cambridge Crystallographic Data Centre under deposition codes 2097583–2097589.

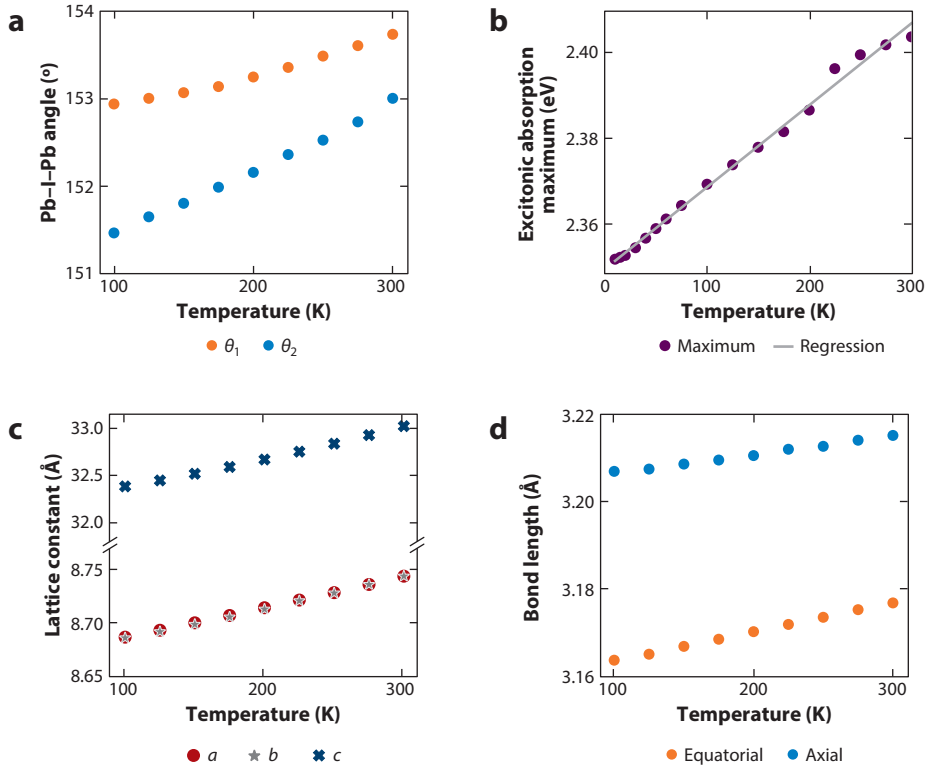

Figure 5

Temperature-dependent structural properties of $(PEA)_2PbI_4$ [PEA: phenethylammonium ($C_6H_5C_2H_4NH_3^+$)]. Temperature-dependent change in (*a*) Pb–I–Pb bond angles θ_1 (*orange circles*) and θ_2 (*blue circles*); (*b*) excitonic absorption maximum (*purple circles*) with linear regression (*gray line*); (*c*) *a* (*red circles*), *b* (*gray stars*), and *c* (*dark blue crosses*) lattice constants; (*d*) equatorial (*orange circles*) and axial (*blue circles*) Pb–I bond lengths.

A common feature of oxide and halide perovskites is that they become less distorted and the unit cell volume increases as the temperature increases (12), and this is also observed for $(PEA)_2PbI_4$. The Pb–I–Pb bond angles increase and the inorganic framework becomes less distorted as the 2DHP is warmed (**Figure 5*a***), which (based on the discussion in Section 3.2) should lead to a reduction in band gap. In most semiconductors, the band gap decreases in energy as the temperature is increased. However, here the opposite temperature dependence is observed: The excitonic absorption maximum increases in energy upon warming (**Figure 5*b***) (37, 52). This phenomenon is also seen in 3DHPs as well as in lead chalcogenide semiconductors (78, 79).

In the 3DHP methylammonium lead iodide, the blue-shift upon warming was thermodynamically attributed to the large increase in unit cell volume as the temperature rises (79). We believe that this phenomenon warrants further study, because the structural changes are more subtle than what can be inferred solely from examining the volume. While the volume of the inorganic framework increases, which can be seen by the increase in *a* and *b* lattice constants (**Figure 5*c***), virtually all the volume increase can be attributed to an increase in Pb–I–Pb bond angle, because the Pb–I bonds do not significantly elongate as the temperature increases (**Figure 5*d***). The lack of Pb–I bond elongation is not unique to $(PEA)_2PbI_4$. Indeed, in the 3D inorganic halide perovskite $CsPbI_3$, the Pb–I bond lengths decrease as the temperature increases, even though the overall unit

cell volume increases (17, 80). We hypothesize that the widening band gap as the temperature increases is related to the unusual thermal expansion properties, and a careful theoretical analysis is needed to characterize the origins of these structural and electronic phenomena.

4. ENERGETIC DISORDER CAUSED BY THE FREE VOLUME IN THE ORGANIC FRAMEWORK

Even when the cation does not induce significant structural distortion, leaving the exciton binding energy and band gap unchanged, significant changes in the optical spectra can be found. For example, in the $(4\text{-XPEA})_2PbI_4$ (X = H, F, Cl, Br, or CH_3) family, lengthening the PEA cation by introducing a larger substituent in the 4-position of the phenyl group increases the interlayer Pb–Pb spacing (*d*; **Figure 1*c*,*d***). However, it does not significantly distort the inorganic framework, as seen by the invariance in the Pb–I–Pb bond angle and excitonic absorption maximum (37) (**Figure 4*e*,*f***).

As the cation is lengthened, the excitonic absorption resonance significantly broadens at both room temperature (**Figure 6*a***) and 10 K (37) (**Figure 6*b***). The broadening implies that longer (but not heavier, as CH_3 is lighter than Cl) cations create significant energetic disorder. To quantify the effect of cation substitution on the excitonic absorption resonance, the temperature-dependent line width (**Figure 6*c***) is fit to a model that accounts for vibration-induced line width broadening developed for transition-metal dichalcogenides (81) but is also applied in 2D and 3DHPs (37, 82–84). The line width $\Gamma(T)$ is fit to the equation

$$\Gamma(T) = \Gamma(0) + \frac{\gamma_{LO}}{\exp\left(\frac{E_{LO}}{k_B T}\right) - 1}, \qquad 2.$$

where $\Gamma(0)$ is the zero-temperature line width, γ_{LO} is the electron–phonon coupling strength to LO phonons, and E_{LO} is the energy of the phonon that couples to the exciton (**Figure 6*d***). $\Gamma(0)$ increases as the cation length increases, consistent with greater energetic disorder and a higher effective temperature of the 2DHP. In addition, γ_{LO} significantly decreases as the cation gets longer, indicating that longer cations reduce the electron–phonon coupling strength. The phonon energy E_{LO} is discussed at length in Section 5.

Structurally, longer cations have been shown to increase the volume available to the cation, as larger cations increase the interlayer spacing but do not fill all the additional interstitial space on their own because the 4-XPEA cations are identical in width (**Figure 4*e***). The additional free volume in the organic layer reduces the degree to which the organic cations physically constrain the motion of the inorganic layers (37). The absorption process samples the instantaneous ground-state energy landscape of the 2DHP and the broader excitonic absorption spectra reflect the additional disorder induced by the longer cations. This hypothesis is further supported by the observation that a more rigid organic layer increases the photoluminescence quantum yield and reduces nonradiative recombination, because additional motion of the organic and/or inorganic frameworks may create more nonradiative recombination pathways (85).

In contrast to the excitonic absorption resonance, photoluminescence spectra show no significant increase in line width with changes in cation length (**Figure 6*e*,*f***). Polaron formation (i.e., electron–phonon coupling) in the excited state is hypothesized to stabilize a particular lattice configuration. Excitons in 2DHPs live for several picoseconds before undergoing photoluminescence, and, accordingly, polaron formation funnels the excitons to an energetic minimum before they recombine (37). The difference between these absorption and photoluminescence spectra demonstrates that the ground and excited states of 2DHPs behave differently, which is important to consider when modeling their structural, optical, and electronic properties.

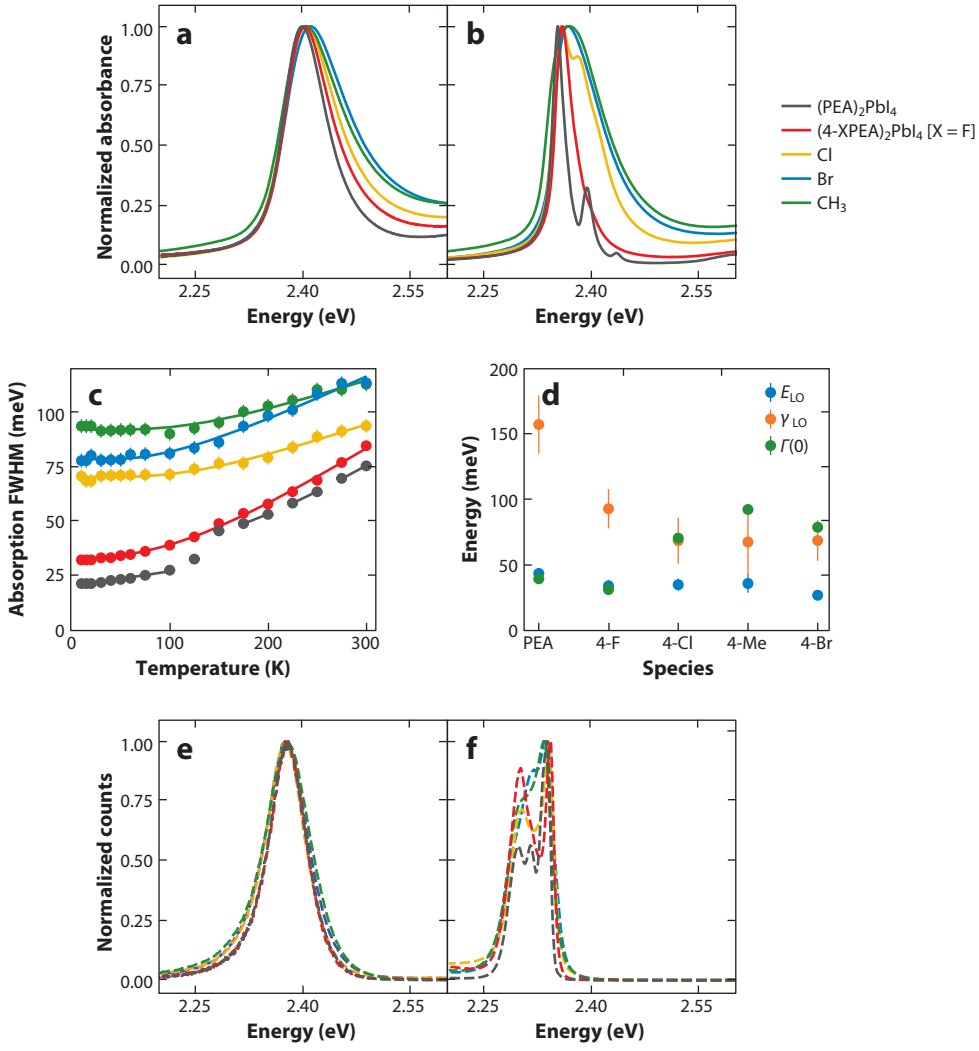

Figure 6

Longer cations and energetic disorder. Absorption spectra at (*a*) 300 K and (*b*) 10 K of $(PEA)_2PbI_4$ (*gray line*), $(4\text{-}XPEA)_2PbI_4$ [X = F (*red line*), Cl (*yellow line*), Br (*blue line*), CH_3 (*green line*)], with (*c*) temperature-dependent FWHM line widths and (*d*) extracted fit parameters. Photoluminescence spectra are also shown at (*e*) 300 K and (*f*) 10 K. Abbreviations: FWHM, full-width at half-maximum; PEA, phenethylammonium ($C_6H_5C_2H_4NH_3^+$). Figure adapted with permission from Reference 37; copyright 2019 American Chemical Society.

Other cation families with tunable lengths do not show length-dependent changes to their optical spectra. For instance, the excitonic absorption spectra of alkylammonium lead iodide $[(C_nH_{2n+1}NH_3)_2PbI_4]$ 2DHPs (**Figure 3*a***) do not broaden as the length of the cation changes (47). We hypothesize that the difference in behavior between the $(C_nH_{2n+1}NH_3)_2PbI_4$ and $(4\text{-}XPEA)_2PbI_4$ 2DHP families originates from the difference in cation geometry, in which unlike $(4\text{-}XPEA)_2PbI_4$, alkylammonium cations have a constant width over their entire length and, thus, do not create additional free volume as their length increases.

5. STRUCTURE IN EXCITONIC OPTICAL SPECTRA AND HOT-EXCITON PHOTOLUMINESCENCE

At temperatures below 100 K, the excitonic absorption and photoluminescence resonances in the archetypal 2DHP $(PEA)_2PbI_4$ split into several discrete resonances (46, 52, 86). This section investigates the origin of this structure as well as how the changes to the cation modify the spacing of the resonances.

5.1. Cryogenic Optical Spectra

Figure 7*a* shows the excitonic absorption and photoluminescence spectra of $(PEA)_2PbI_4$ at a temperature of 15 K (52). In the absorption spectrum, there are three discrete resonances, Ex_{1a} at 2.355 eV, Ex_{1b} at 2.398 eV, and Ex_{1c} at 2.438 eV, that are separated from one another by 40 to 43 meV. These resonances fit to Lorentzian lineshapes, indicating that they are homogeneously broadened (i.e., all excitons experience the same local environment).

In photoluminescence, Ex_{1a} is present along with another strong Stokes-shifted resonance, Ex_2, which is separated from Ex_{1a} by 40 meV. When the photoluminescence spectrum is magnified, two additional resonances appear (**Figure 7*a***) at the same energies as the Ex_{1b} and Ex_{1c} resonances that are seen in absorption (52). These hot photoluminescence resonances are noteworthy because, in most emitters, carriers lose their excess kinetic energy through vibrational relaxation to the lowest-lying excited state before recombining; this principle is known as Kasha's rule (87). Only 0.3% of the photoluminescence in $(PEA)_2PbI_4$ occurs out of these hot states (59). In contrast to the excitonic absorption resonances, the resonances in photoluminescence are best fit with Gaussian functions, indicating that the resonances are inhomogeneously broadened (52). Each exciton, therefore, occupies a different local environment when recombining.

In Sections 5.2–5.4, we describe hypotheses for the origin of the excitonic absorption and photoluminescence resonances labeled Ex_{1a}, Ex_{1b}, and Ex_{1c}. The photoluminescence peak Ex_2 is reported to be a bound exciton (85) or biexciton emission (88–90), as Ex_2 shows a different intensity dependence than does Ex_{1a}. Ex_{1a} scales linearly with excitation density (59) until saturation occurs, and the saturation behavior is hypothesized to be caused by exciton–exciton annihilation (analogous to Auger recombination for free carriers) (85) or biexciton formation (88). In contrast, Ex_2 saturates under continuous illumination (59), while it grows linearly (85) or superlinearly (88) when excited with ultrafast pulsed excitation. We note that there is an additional shoulder in the absorption spectrum, which is consistent with a resonance 14 meV higher in energy, that we do not discuss here (52).

5.2. The Exciton–Phonon Coupling Hypothesis

One hypothesis is that Ex_{1a}, Ex_{1b}, and Ex_{1c} are caused by the coupling of the exciton to a vibrational mode (52, 59, 91, 92). Ultrafast time-resolved photoluminescence measurements (**Figure 7*b*,*c***) are used to observe the fate of photoexcitations in 2DHPs, monitoring the population of the individual excitonic resonances. The population of Ex_{1c} decays while that of Ex_{1b} continues to rise, and, likewise, the population of Ex_{1b} begins to decay while those of Ex_{1a} and Ex_2 continue to increase. The kinetics suggest that a selection rule operates such that excitons cannot relax directly into all states but instead can only relax from the nth to the $n-1$th state, as in the quantum harmonic oscillator (**Figure 7*d***). The equal spacing between resonances combined with the photoluminescence kinetics led us to hypothesize that Ex_{1b} and Ex_{1c} are vibronic replicas of Ex_{1a} caused by the exciton coupling to a ~40-meV phonon (52). Theoretical calculations show that a phonon with this energy must exclusively involve motion of the cation, because modes involving the heavy Pb

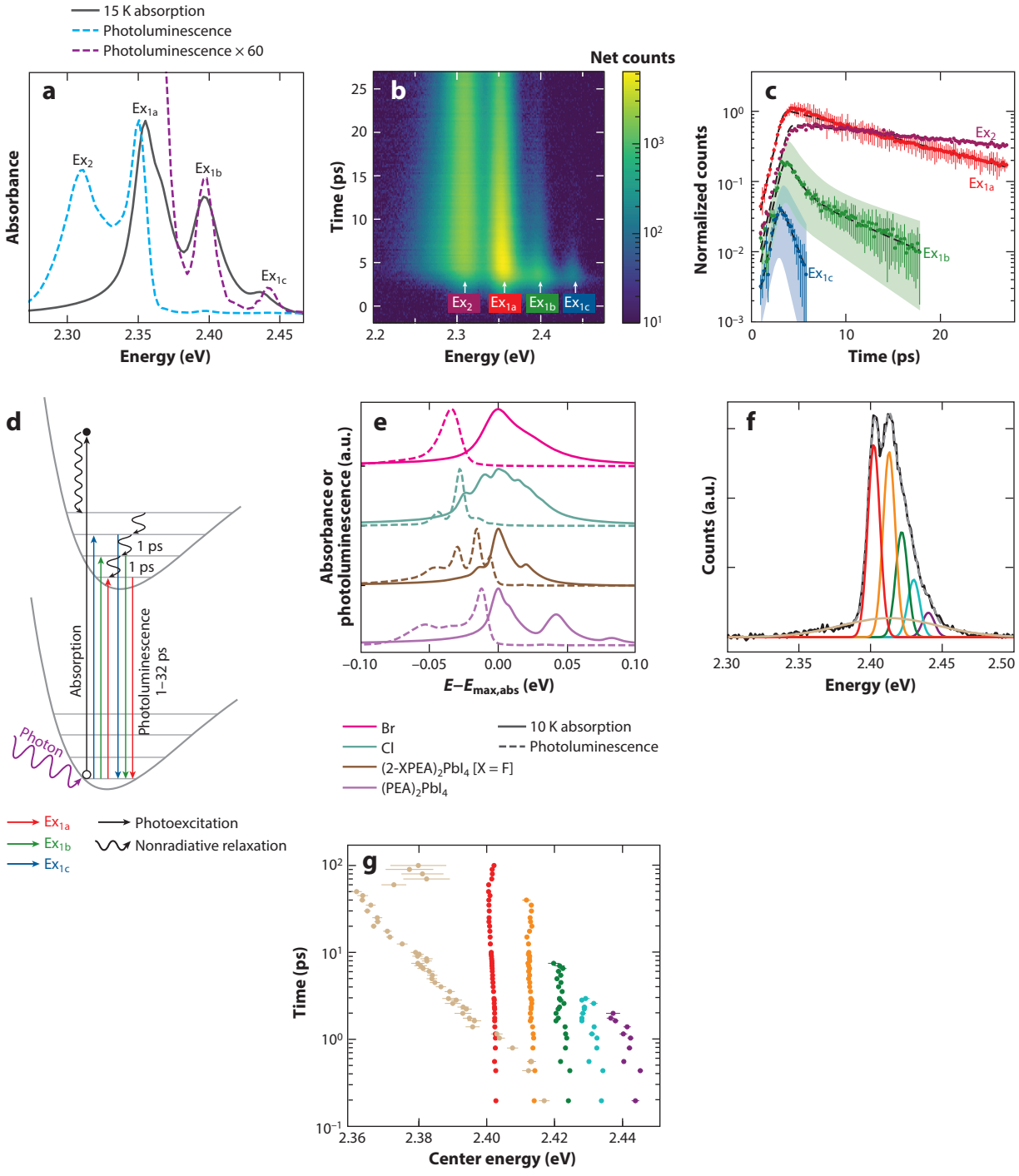

(*Caption appears on following page*)

Figure 7 (*Figure appears on preceding page*)

Discrete excitonic structure in $(PEA)_2PbI_4$. (*a*) Shows 15 K absorption (*gray solid line*) and photoluminescence (*blue dashed line*; × 60 *purple dashed line*) and (*b*) time-resolved photoluminescence. (*c*) Lifetime fit of integrated amplitude of photoluminescence resonances shown in panel *b*. (*d*) Schematic detailing low-temperature absorption and photoluminescence processes for Ex_{1a} (*red arrows*), Ex_{1b} (*green arrows*), and Ex_{1c} (*blue arrows*). Nonradiative relaxation between vibrational states is shown by black wavy arrows. Panels *a–d* adapted with permission from Reference 52; copyright 2016 American Chemical Society. (*e*) 10 K absorption (*solid lines*) and photoluminescence (*dashed lines*) of $(PEA)_2PbI_4$ (*purple*) and $(2\text{-XPEA})_2PbI_4$ [X = F (*brown*), Cl (*green*), and Br (*magenta*)]. (*f*) Fit of ultrafast time-resolved photoluminescence spectrum of $(2\text{-ClPEA})_2PbI_4$ taken at $t = 0.55$ ps. (*g*) Energies of resonances found by fitting each time step of the time-resolved photoluminescence spectrum of $(2\text{-ClPEA})_2PbI_4$. Panels *e–g* adapted with permission from Reference 59; copyright 2020 American Chemical Society. Abbreviations: abs, absorbance; max, maximum; PEA, phenethylammonium ($C_6H_5C_2H_4NH_3^+$).

and I atoms are all much lower in energy. The responsible phonon likely involves a twisting of the phenyl group (52).

In addition to the splitting of the absorption and photoluminescence spectra and the photoluminescence kinetics, other evidence supports the assignment of a vibronic progression. Magneto-optical measurements show an identical shift with the presence of a magnetic field for all resonances, indicating that the discrete resonances all have the same origin (92). As the temperature increases, Ex_{1a}, Ex_{1b}, and Ex_{1c} in absorption merge into a single resonance (**Figure 6*e***). Using Equation 2 and fitting the exciton absorption line width of $(PEA)_2PbI_4$ from 175 to 300 K, the optical phonon that broadens the exciton was found to have an energy E_{LO} of 43 meV, matching the energetic spacing between Ex_{1a}, Ex_{1b}, and Ex_{1c} at 15 K (37) (**Figure 6*c,d***). In addition, $(PEA)_2PbI_4$ exhibits strong electron–phonon coupling to this vibration, with a coupling constant γ_{LO} of 160 meV, four times greater than that of lead iodide 3DHPs (82). Fitting the photoluminescence spectrum from 125 to 300 K to Equation 2 gives similar results, yielding a phonon energy E_{LO} of 45 meV and an electron–phonon coupling constant γ_{LO} of 190 meV. We separately extracted the absorption line width of Ex_{1a} from lower, 10–100 K temperature spectra, in which it is resolved separately from the thermally broadened absorption envelope that contains Ex_{1a}, Ex_{1b}, and Ex_{1c}. Fitting Ex_{1a} at lower temperature, we found E_{LO} is 6.9 meV and γ_{LO} is 8 meV, showing that Ex_{1a} on its own weakly couples to a low-energy phonon distinct from the phonon involved in the vibronic progression (37). We note that other groups have fit the line width of the entire photoluminescence spectrum from ∼10 to 300 K in a single regression and found $E_{LO} =$ 17 or 18 meV and $\gamma_{LO} = 25$ or 43 meV (83, 91), values that are in between those we found when separately fitting the high- and low-temperature regimes. We hypothesize that fitting the entire spectrum averages the low- and high-temperature regimes, which we do not believe to be accurate given that the discrete resonances are only resolved at temperatures below 100 K in $(PEA)_2PbI_4$.

5.3. Testing the Exciton–Phonon Coupling Hypothesis Through Cation Substitution

The phonon that couples to the exciton was hypothesized to reside on the organic cation. Thus, modifying the cation is expected to alter the energy of the phonon that couples to the exciton. The energy of a normal stretching vibration is inversely proportional to the mass of the vibrating atoms. In a twisting mode, the mass is replaced with the moment of inertia, which quantifies how far the mass is from the rotational axis. Accordingly, if mass is added close to the rotational axis, the moment of inertia and, therefore, the energy of a twisting vibration hardly changes. If mass is added far from the rotational axis, the energy of the vibration is greatly decreased.

We hypothesized that the rotational axis passes through the 1,4-axis of the PEA cation, parallel to the ethylammonium tether. We therefore synthesized and spectroscopically measured $(4\text{-XPEA})_2PbI_4$ derivatives, adding mass close to the rotational axis, and $(2\text{-XPEA})_2PbI_4$

derivatives, adding mass away from the rotational axis, to identify the nature of the vibrational mode that couples to the exciton. While the increased energetic disorder in $(4\text{-XPEA})_2PbI_4$ washes out the excitonic structure, consistent with weaker electron–phonon coupling (Section 4), using Equation 2 to fit the excitonic absorption line widths, we found that E_{LO} decreases from 43 meV for unsubstituted $(PEA)_2PbI_4$ by 19% to 34–36 meV for X = F, Cl, and Me, and by 37% to 27 meV for X = Br (37). The changes in the phonon energy are small considering that the mass of the 4-position substituent increases from 1 amu (unsubstituted PEA) to 85 amu (4-BrPEA), suggesting the vibrational mode that couples to the exciton is a twisting mode of the cation.

The photophysics of $(2\text{-XPEA})_2PbI_4$ derivatives show much more extreme changes with single-atom substitutions on the cation (59). Multiple excitonic resonances are observed in their low-temperature absorption and photoluminescence spectra, which we used to directly quantify the energy of the phonon that couples to the exciton (**Figure 7*e***). Ultrafast photoluminescence measurements, similar to those in **Figure 7*b*,*c***, were collected to monitor the kinetics and identify excitonic resonances and their vibronic replicas. In $(2\text{-FPEA})_2PbI_4$ (**Figure 7*e***), the photoluminescence kinetics suggest that there are two distinct manifolds of states, with the resonances in each manifold separated from one another by 20–24 meV (59). We hypothesized that the presence of two manifolds of states is caused by asymmetry in the inorganic lattice, where there are two distinct Pb–I–Pb bond angles that differ by ∼3° from one another.

In $(2\text{-ClPEA})_2PbI_4$ (**Figure 7*e***), we found one manifold of states in which the states are separated by 12–13 meV from one another, consistent with the symmetric inorganic framework of $(2\text{-ClPEA})_2PbI_4$ only having a single Pb–I–Pb bond angle, in contrast with the asymmetric lattice of $(2\text{-FPEA})_2PbI_4$. The smaller spacing between resonances in $(2\text{-ClPEA})_2PbI_4$ compared to those in $(2\text{-FPEA})_2PbI_4$ is consistent with the heaver Cl atom resulting in a larger moment of inertia and, therefore, a smaller vibrational energy than that of the 2-FPEA cation. In time-resolved photoluminescence spectra, we were able to identify five discrete states, four of which are hot (**Figure 7*f*,*g***). The fractions of hot-exciton photoluminescence in $(2\text{-FPEA})_2PbI_4$ and $(2\text{-ClPEA})_2PbI_4$ are 9.8% and 8.4%, respectively, more than an order of magnitude greater than in unsubstituted $(PEA)_2PbI_4$. No excitonic structure was observed in $(2\text{-BrPEA})_2PbI_4$ (**Figure 7*e***), which we hypothesize is either caused by the heavy Br atom reducing the phonon energy such that discrete resonances blend together or caused by the highly distorted, corrugated inorganic framework altering the optical properties. The much smaller splitting between resonances in $(2\text{-XPEA})_2PbI_4$ supports the hypothesis that the excitonic structure is caused by coupling to a twisting mode of the PEA cation because the addition of mass far from the rotational axis of the phenyl group greatly decreases the energy between resonances in the excitonic absorption and photoluminescence spectra. Hot photoluminescence resonances separated from the central resonance by 15 meV were also found in $(3\text{-FPEA})_2PbI_4$ (91), which is also consistent with this hypothesis.

5.4. Criticism of the Exciton–Phonon Coupling Hypothesis

The hypothesis that the excitonic structure in $(PEA)_2PbI_4$ and its derivatives is caused by coupling to a phonon is controversial (93) for several reasons. The first reason is that there is no mirror symmetry between the excitonic absorption and photoluminescence spectra. In a typical molecular vibronic progression, the absorption resonances are mirrored in photoluminescence about the zero-phonon line (Ex_{1a} in **Figure 7*a***) (94). This mirror symmetry is imposed by the Franck-Condon approximation, which states that electronic transition probabilities do not depend on the nuclear coordinates (95). According to the Franck-Condon principle, in $(PEA)_2PbI_4$, we would expect to observe replicas of Ex_{1b} and Ex_{1c} at lower energy than Ex_{1a} in photoluminescence, which

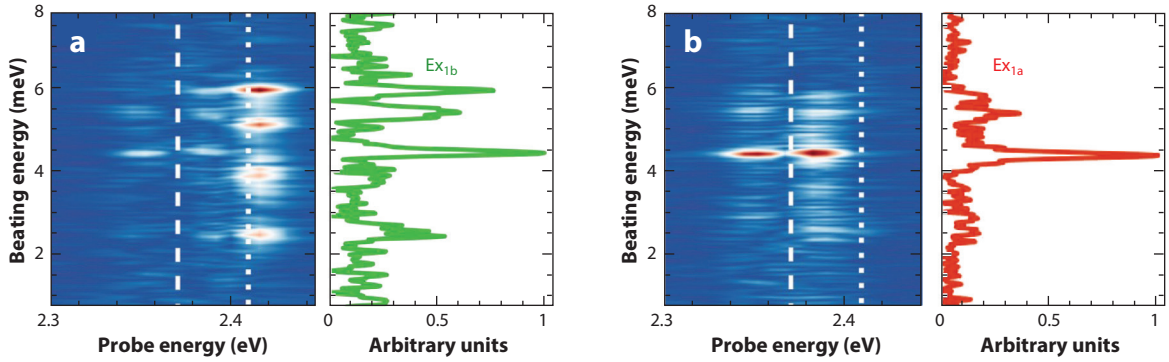

Figure 8

Exciton–phonon coupling details for (*a*) Ex_{1b} and (*b*) Ex_{1a} in an excited state, showing (*left*) the two-dimensional resonant impulsive stimulated Raman scattering spectra (*right*) integrated over detection energy. Figure adapted with permission from Reference 93; copyright 2020 American Chemical Society.

is not what is observed. However, 3D lead halide perovskites are known to undergo structural changes to their lattice on a picosecond timescale upon photoexcitation (96, 97). To the best of our knowledge, light-induced structural changes have not been studied in 2DHPs but, given the similarity to 3DHPs, we expect this phenomenon to be present. Structural changes to the lattice would invalidate the Franck-Condon approximation, so mirror symmetry would no longer be expected.

The second major criticism of the vibronic coupling hypothesis is that in $(PEA)_2PbI_4$, Ex_{1a} and Ex_{1b} were found to couple differently to low energy (1–8 meV) phonons located on the inorganic framework. **Figure 8** shows resonant impulsive stimulated Raman spectra when either Ex_{1b} (**Figure 8*a***) or Ex_{1a} (**Figure 8*b***) is excited (93, 98). The 2D Raman spectra are generated by Fourier transforming the transient absorption spectra. If Ex_{1b} were a vibronic replica of Ex_{1a}, the resonances would be expected to couple similarly to the inorganic lattice, yet the Raman spectra differ (93). Instead, it was hypothesized that Ex_{1a}, Ex_{1b}, Ex_{1c}, and Ex_2 are separate but correlated excitons that each have different binding energies (93, 98).

We suggest that the difference in coupling between Ex_{1b} and Ex_{1a} to the inorganic lattice can be explained by the different lifetimes of the individual resonances. At 15 K, photoluminescence from Ex_{1b} (**Figure 7*c***) has a lifetime of 2 ps, whereas photoluminescence from Ex_{1a} has a lifetime of 13 ps (52). As structural reorganization of the inorganic lattice likely occurs on a picosecond timescale, Ex_{1b} likely decays before the lattice reorganization is complete. Therefore, Ex_{1b} perceives a different inorganic lattice configuration than does Ex_{1a}, and the vibrational spectrum as well as the exciton–phonon coupling dynamics may change as the lattice reconfigures.

We agree that Ex_2 likely has a different origin than Ex_{1a}, Ex_{1b}, and Ex_{1c} because of its different pump intensity dependence. However, it is too coincidental for Ex_{1a}, Ex_{1b}, and Ex_{1c} to be distinct excitons with their own binding energy and yet be separated from one another by a constant energy with dynamics that obey the vibrational selection rule. Furthermore, the agreement of E_{LO} from line width analysis (**Figure 6*d***) with the spacing between Ex_{1a}, Ex_{1b}, and Ex_{1c} is consistent with the exciton coupling to a vibration on the organic cation. Finally, the ability to tune the excitonic structure through cation substitutions as well as the existence of five discrete excitonic resonances with equal separation in $(2\text{-ClPEA})_2PbI_4$ (**Figure 7*f*,*g***) further supports the existence of a vibronic progression. 2DHPs have very complicated exciton dynamics, and further study is needed to confirm the origins of the low-temperature excitonic structure.

6. CONCLUSION

A large library of organic cations can be introduced to synthesize stoichiometric crystal(lite)s of 2DHPs with tremendous diversity in structural (25), optical, and electronic (34, 99) properties. The geometry (i.e., length and width) and the chemistry of the organic cation can alter the structure and dielectric environment of the inorganic framework, with most cations establishing a large spacing such that the inorganic layers are strongly quantum confined and also weakly electronically coupled. 2DHPs have some unconventional optical properties in comparison to other longer-studied inorganic or organic semiconductors. Through systematic modifications of the organic cation, the community has synthesized, structurally characterized, and spectroscopically studied semiconducting 2DHPs to begin to uncover their unusual yet fascinating photophysics. Even for aliphatic or short aromatic ammonium cations that create Type I heterostructures in which excitons reside in the inorganic framework, at a distance, the organic cation can modify the energy, line width, and population dynamics of excitonic states. Near the band gap energy, low-temperature optical spectra of many 2DHPs show multiple excitonic resonances with ultrafast, picosecond photoluminescence lifetimes that are comparable to vibrational relaxation timescales, consistent with a breakdown in the Franck-Condon approximation, and give rise to hot-exciton luminescence in violation of Kasha's rule.

As scientists, we make wish lists about capabilities and knowledge. For 2DHPs, one item on our list would be to carry out single-crystal diffraction measurements at the ~10–15 K temperatures at which thermal broadening and thus line widths in optical spectra are reduced to resolve multiple excitonic resonances. This would allow more detailed correlation of structure and properties and the identification of first- and second-order phase transitions, and it would build confidence in spectral assignments. Advances in optical and vibrational spectroscopies have allowed greater sophistication in our ability to probe materials (95) and are being used to study 2DHPs. Uniting the community and its capabilities to map the similarities and differences in the energy, intensities, and timescales across techniques promises to address the differences in our observations and controversies in our analyses about excitonic and vibrational processes. Collaboration between experiment and theory to measure and model 2DHPs, particularly the dynamics in the excited state, is important in these materials that are soft and known to reorganize in response to carriers and excitons.

The relationships between structure and properties are critical for establishing design rules that allow us to exploit the chemical diversity of these 2DHPs and their large exciton binding energy, which make them excellent candidates for excitonic devices. These devices include heterojunction solar cells and photodetectors (100, 101), efficient fluorophores and light-emitting diodes that emit spectrally narrow (102, 103) or broad-spectrum white (104) light, as the gain medium in lasers (7, 105), and narrow bandwidth optical modulators. Despite the large binding energy, the photoluminescence quantum yield rapidly decays at temperatures above 200 K in many 2DHPs (46, 106). In Type I 2DHPs (34, 107), efficient electroluminescence has only been achieved at temperatures <200 K (102, 103). The decrease in radiative recombination near room temperature has been attributed to thermal dissociation of excitons and strong electron–phonon coupling leading to rapid nonradiative recombination (3, 46, 102, 103, 106, 108). Fully understanding the relationship between the structure of 2D perovskites and the resulting electronic/excitonic coupling to phonons is important to realize their promise as emissive materials. Slow carrier cooling in 2DHPs may allow hot carriers to be extracted before relaxing to the lowest-lying state (109, 110), and it may be possible to further slow excitonic relaxation by tuning the cation. Slowing vibrational relaxation may also allow for population inversion and make 2DHPs suitable gain material in lasers (82, 105). The atomic-scale perfection of the inorganic framework and the

large binding energy in absorption suggest 2DHPs should enable ultrasharp optical modulators (111), but the realization of this application requires minimizing the sources of energetic disorder that broaden the absorption line width. In addition to conventional devices, these unique properties make 2D perovskites a promising platform for exotic devices that use excitonics for energy transfer and communication, such as a photonic wire that harnesses the energetic properties of excitons for directional transmission of energy (112) or novel polaritonic devices (113) such as optical transistors and circuits that require strong exciton–photon coupling (114).

DISCLOSURE STATEMENT

The authors are not aware of any affiliations, memberships, funding, or financial holdings that might be perceived as affecting the objectivity of this review.

ACKNOWLEDGMENTS

We thank Michael R. Gau and Patrick J. Carroll for performing the temperature-dependent single-crystal X-ray diffraction measurements of $(PEA)_2PbI_4$. This work is supported by C.R.K.'s Stephen J. Angello Professorship.

LITERATURE CITED

1. Kittel C. 2005. *Introduction to Solid State Physics*. Hoboken, NJ: Wiley. 8th ed.
2. Pankove JI. 1975. *Optical Processes in Semiconductors*. Dover Books Explain. Sci, Vol. 119. New York: Dover Publ.
3. Sze SM, Ng KK. 2007. *Physics of Semiconductor Devices*. Hoboken, NJ: Wiley-Intersci. 3rd ed.
4. Pope M, Swenberg CE. 1999. *Electronic Processes in Organic Crystals and Polymers*. New York: Oxford Univ. Press. 2nd ed.
5. Murray CB, Kagan CR, Bawendi MG. 2000. Synthesis and characterization of monodisperse nanocrystals and close-packed nanocrystal assemblies. *Annu. Rev. Mater. Sci.* 30:545–610
6. Kagan CR, Lifshitz E, Sargent EH, Talapin DV. 2016. Building devices from colloidal quantum dots. *Science* 353(6302):science.aac5523
7. Saparov B, Mitzi DB. 2016. Organic-inorganic perovskites: structural versatility for functional materials design. *Chem. Rev.* 116(7):4558–96
8. Straus DB, Kagan CR. 2018. Electrons, excitons, and phonons in two-dimensional hybrid perovskites: connecting structural, optical, and electronic properties. *J. Phys. Chem. Lett.* 9(6):1434–47
9. Momma K, Izumi F. 2011. VESTA 3 for three-dimensional visualization of crystal, volumetric and morphology data. *J. Appl. Crystallogr.* 44(6):1272–76
10. Møller C. 1958. Crystal structure and photoconductivity of cæsium plumbohalides. *Nature* 182(4647):1436
11. Wells HL. 1893. Über die Cäsium- und Kalium-Bleihalogenide [About the cesium and potassium lead halides]. *Z. Anorg. Chem.* 3(1):195–210
12. Mitchell RH. 2002. *Perovskites: Modern and Ancient*. Thunder Bay, Can.: Almaz Press
13. Goldschmidt VM. 1926. Die Gesetze der Krystallochemie [The laws of crystal chemistry]. *Naturwissenschaften* 14(21):477–85
14. Goldschmidt VM. 1929. Crystal structure and chemical constitution. *Trans. Faraday Soc.* 25:253
15. Filip MR, Giustino F. 2018. The geometric blueprint of perovskites. *PNAS* 115(21):5397–402
16. Hellenbrandt M. 2004. The Inorganic Crystal Structure Database (ICSD)—present and future. *Crystallogr. Rev.* 10(1):17–22
17. Straus DB, Guo S, Abeykoon AM, Cava RJ. 2020. Understanding the instability of the halide perovskite $CsPbI_3$ through temperature-dependent structural analysis. *Adv. Mater.* 32(32):2001069
18. Weber D. 1979. Das Perowskitsystem CH_3NH_3 [Pb,Sn_{1-n} X3] (X = Cl, Br, I) /The perovskite system CH_3NH_3 [Pb,Sn_{1-n} X3] (X = C1, Br, I). *Z. Naturforsch. B* 34(7):939–41

19. Weber D. 1978. $CH_3NH_3PbX_3$, ein Pb(II)-System mit kubischer Perowskitstruktur /$CH_3NH_3PbX_3$, a Pb(II)-system with cubic perovskite structure. *Z. Naturforsch. B* 33(12):1443–45
20. Kojima A, Teshima K, Shirai Y, Miyasaka T. 2009. Organometal halide perovskites as visible-light sensitizers for photovoltaic cells. *J. Am. Chem. Soc.* 131(17):6050–51
21. Green MA, Ho-Baillie A, Snaith HJ. 2014. The emergence of perovskite solar cells. *Nat. Photon.* 8(7):506–14
22. Natl. Renew. Energy Lab. 2018. Best research-cell efficiencies. *National Renewable Energy Laboratory*. **http://www.nrel.gov/pv/assets/images/efficiency-chart.png**
23. Mitzi DB, Feild CA, Harrison WTA, Guloy AM. 1994. Conducting tin halides with a layered organic-based perovskite structure. *Nature* 369(6480):467–69
24. Mitzi DB. 1999. Synthesis, structure, and properties of organic-inorganic perovskites and related materials. In *Progress in Inorganic Chemistry*, Vol. 48, ed. KD Karlin, pp. 1–121. Hoboken, NJ: Wiley
25. McNulty JA, Lightfoot P. 2021. Structural chemistry of layered lead halide perovskites containing single octahedral layers. *IUCrJ* 8(4):485–513
26. Tremblay M-H, Bacsa J, Zhao B, Pulvirenti F, Barlow S, Marder SR. 2019. Structures of (4-Y-$C_6H_4CH_2NH_3)_2PbI_4$ {Y = H, F, Cl, Br, I}: tuning of hybrid organic inorganic perovskite structures from Ruddlesden–Popper to Dion–Jacobson limits. *Chem. Mater.* 31(16):6145–53
27. Mitzi DB. 1996. Synthesis, crystal structure, and optical and thermal properties of $(C_4H_9NH_3)_2MI_4$ (M = Ge, Sn, Pb). *Chem. Mater.* 8(3):791–800
28. Mauck CM, Tisdale WA. 2019. Excitons in 2D organic-inorganic halide perovskites. *Trends Chem.* 1(4):380–93
29. Hoffmann R. 1987. How chemistry and physics meet in the solid state. *Angew. Chem. Int. Ed.* 26(9):846–78
30. Pierret RF. 2003. *Advanced Semiconductor Fundamentals*. Upper Saddle River, NJ: Prentice Hall. 2nd ed.
31. Even J, Pedesseau L, Katan C. 2014. Understanding quantum confinement of charge carriers in layered 2D hybrid perovskites. *Chem. Phys. Chem.* 15(17):3733–41
32. Gebhardt J, Kim Y, Rappe AM. 2017. Influence of the dimensionality and organic cation on crystal and electronic structure of organometallic halide perovskites. *J. Phys. Chem. C* 121(12):6569–74
33. Even J, Pedesseau L, Dupertuis M-A, Jancu J-M, Katan C. 2012. Electronic model for self-assembled hybrid organic/perovskite semiconductors: reverse band edge electronic states ordering and spin-orbit coupling. *Phys. Rev. B* 86(20):205301
34. Mitzi DB, Chondroudis K, Kagan CR. 2001. Organic-inorganic electronics. *IBM J. Res. Dev.* 45(1):29–45
35. Pedesseau L, Sapori D, Traore B, Robles R, Fang H-H, et al. 2016. Advances and promises of layered halide hybrid perovskite semiconductors. *ACS Nano* 10(11):9776–86
36. Smith MD, Pedesseau L, Kepenekian M, Smith IC, Katan C, et al. 2017. Decreasing the electronic confinement in layered perovskites through intercalation. *Chem. Sci.* 8(3):1960–68
37. Straus DB, Iotov N, Gau MR, Zhao Q, Carroll PJ, Kagan CR. 2019. Longer cations increase energetic disorder in excitonic 2D hybrid perovskites. *J. Phys. Chem. Lett.* 10(6):1198–205
38. Katan C, Mercier N, Even J. 2019. Quantum and dielectric confinement effects in lower-dimensional hybrid perovskite semiconductors. *Chem. Rev.* 119(5):3140–92
39. Keldysh LV. 1979. Coulomb interaction in thin semiconductor and semimetal films. *JETP Lett.* 29(11):658–61
40. Tanaka K, Takahashi T, Kondo T, Umebayashi T, Asai K, Ema K. 2005. Image charge effect on two-dimensional excitons in an inorganic-organic quantum-well crystal. *Phys. Rev. B* 71(4):045312
41. Hanamura E, Nagaosa N, Kumagai M, Takagahara T. 1988. Quantum wells with enhanced exciton effects and optical non-linearity. *Mater. Sci. Eng. B* 1(3–4):255–58
42. Raja A, Chaves A, Yu J, Arefe G, Hill HM, et al. 2017. Coulomb engineering of the bandgap and excitons in two-dimensional materials. *Nat. Commun.* 8:15251
43. Sutton RJ, Filip MR, Haghighirad AA, Sakai N, Wenger B, et al. 2018. Cubic or orthorhombic? Revealing the crystal structure of metastable black-phase $CsPbI_3$ by theory and experiment. *ACS Energy Lett.* 3(8):1787–94

44. Galkowski K, Mitioglu A, Miyata A, Plochocka P, Portugall O, et al. 2016. Determination of the exciton binding energy and effective masses for methylammonium and formamidinium lead tri-halide perovskite semiconductors. *Energy Environ. Sci.* 9(3):962–70
45. Pedesseau L, Jancu JM, Rolland A, Deleporte E, Katan C, Even J. 2014. Electronic properties of 2D and 3D hybrid organic/inorganic perovskites for optoelectronic and photovoltaic applications. *Opt. Quantum Electron.* 46(10):1225–32
46. Hong X, Ishihara T, Nurmikko AV. 1992. Dielectric confinement effect on excitons in PbI_4-based layered semiconductors. *Phys. Rev. B* 45(12):6961–64
47. Ishihara T, Takahashi J, Goto T. 1990. Optical properties due to electronic transitions in two-dimensional semiconductors $(AC_nH_{2n+1}NH_3)_2PbI_4$. *Phys. Rev. B* 42(17):11099–107
48. Mathieu H, Lefebvre P, Christol P. 1992. Simple analytical method for calculating exciton binding energies in semiconductor quantum wells. *Phys. Rev. B* 46(7):4092–101
49. Esaki L, Tsu R. 1970. Superlattice and negative differential conductivity in semiconductors. *IBM J. Res. Dev.* 14(1):61–65
50. Even J, Pedesseau L, Katan C, Kepenekian M, Lauret J-S, et al. 2015. Solid state physics perspective on hybrid perovskite semiconductors. *J. Phys. Chem. C* 119(19):10161–77
51. Knutson JL, Martin JD, Mitzi DB. 2005. Tuning the band gap in hybrid tin iodide perovskite semiconductors using structural templating. *Inorg. Chem.* 44(13):4699–705
52. Straus DB, Hurtado Parra S, Iotov N, Gebhardt J, Rappe AM, et al. 2016. Direct observation of electron-phonon coupling and slow vibrational relaxation in organic-inorganic hybrid perovskites. *J. Am. Chem. Soc.* 138(42):13798–801
53. Lin CW, Liu F, Chen TY, Lee KH, Chang CK, et al. 2020. Structure-dependent photoluminescence in low-dimensional ethylammonium, propylammonium, and butylammonium lead iodide perovskites. *ACS Appl. Mater. Interfaces* 12(4):5008–16
54. Im J, Chung J, Kim S, Park N. 2012. Synthesis, structure, and photovoltaic property of a nanocrystalline 2H perovskite-type novel sensitizer $(CH_3CH_2NH_3)PbI_3$. *Nanoscale Res. Lett.* 7(1):353
55. Sourisseau S, Louvain N, Bi W, Mercier N, Rondeau D, et al. 2007. Reduced band gap hybrid perovskites resulting from combined hydrogen and halogen bonding at the organic–inorganic interface. *Chem. Mater.* 19(3):600–7
56. Yaffe O, Chernikov A, Norman ZM, Zhong Y, Velauthapillai A, et al. 2015. Excitons in ultrathin organic-inorganic perovskite crystals. *Phys. Rev. B* 92(4):045414
57. Mao L, Ke W, Pedesseau L, Wu Y, Katan C, et al. 2018. Hybrid Dion-Jacobson 2D lead iodide perovskites. *J. Am. Chem. Soc.* 140(10):3775–83
58. Li Y, Milić JV, Ummadisingu A, Seo JY, Im JH, et al. 2019. Bifunctional organic spacers for formamidinium-based hybrid Dion-Jacobson two-dimensional perovskite solar cells. *Nano Lett.* 19(1):150–57
59. Straus DB, Hurtado Parra S, Iotov N, Zhao Q, Gau MR, et al. 2020. Tailoring hot exciton dynamics in 2D hybrid perovskites through cation modification. *ACS Nano* 14(3):3621–29
60. Tremblay M-H, Bacsa J, Barlow S, Marder SR. 2020. Exciton-band tuning induced by the width of the cation in 2D lead iodide perovskite hybrids. *Mater. Chem. Front.* 4(7):2023–28
61. Papavassiliou GC, Mousdis GA, Raptopoulou CP, Terzis A. 1999. Preparation and characterization of $[C_6H_5CH_2NH_3]_2PbI_4$, $[C_6H_5CH_2CH_2SC(NH_2)_2]_3PbI_5$ and $[C_{10}H_7CH_2NH_3]PbI_3$ organic-inorganic hybrid compounds. *Z. Naturforsch. B* 54(11):1405–9
62. Hu J, Oswald IWH, Stuard SJ, Nahid MM, Zhou N, et al. 2019. Synthetic control over orientational degeneracy of spacer cations enhances solar cell efficiency in two-dimensional perovskites. *Nat. Commun.* 10:1276
63. Billing DG, Lemmerer A. 2007. Synthesis, characterization and phase transitions in the inorganic-organic layered perovskite-type hybrids $[(C_nH_{2n+1}NH_3)_2PbI_4]$, $n = 4$, 5 and 6. *Acta Crystallogr. Sect. B* 63(5):735–47
64. Lemmerer A, Billing DG. 2012. Synthesis, characterization and phase transitions of the inorganic-organic layered perovskite-type hybrids $[(C_nH_{2n+1}NH_3)_2PbI_4]$, $n = 7$, 8, 9 and 10. *Dalt. Trans.* 41(4):1146–57

65. Mauck CM, France-Lanord A, Hernandez Oendra AC, Dahod NS, Grossman JC, Tisdale WA. 2019. Inorganic cage motion dominates excited-state dynamics in 2D-layered perovskites $(C_xH_{2x+1}NH_3)_2PbI_4$ ($x = 4$–9). *J. Phys. Chem. C* 123(45):27904–16
66. Alvarez S. 2013. A cartography of the van der Waals territories. *Dalt. Trans.* 42(24):8617–36
67. Du K-Z, Tu Q, Zhang X, Han Q, Liu J, et al. 2017. Two-dimensional lead(II) halide-based hybrid perovskites templated by acene alkylamines: crystal structures, optical properties, and piezoelectricity. *Inorg. Chem.* 56(15):9291–302
68. Billing DG, Lemmerer A. 2006. Synthesis and crystal structures of inorganic-organic hybrids incorporating an aromatic amine with a chiral functional group. *CrystEngComm* 8(9):686–95
69. Long G, Sabatini R, Saidaminov MI, Lakhwani G, Rasmita A, et al. 2020. Chiral-perovskite optoelectronics. *Nat. Rev. Mater.* 5(6):423–39
70. Ahn J, Lee E, Tan J, Yang W, Kim B, Moon J. 2017. A new class of chiral semiconductors: chiral-organic-molecule-incorporating organic-inorganic hybrid perovskites. *Mater. Horizons* 4(5):851–56
71. Wang L, Xue Y, Cui M, Huang Y, Xu H, et al. 2020. A chiral reduced-dimension perovskite for an efficient flexible circularly polarized light photodetector. *Angew. Chem. Int. Ed.* 59(16):6442–50
72. Lu H, Xiao C, Song R, Li T, Maughan AE, et al. 2020. Highly distorted chiral two-dimensional tin iodide perovskites for spin polarized charge transport. *J. Am. Chem. Soc.* 142(30):13030–40
73. Ma J, Fang C, Chen C, Jin L, Wang J, et al. 2019. Chiral 2D perovskites with a high degree of circularly polarized photoluminescence. *ACS Nano* 13(3):3659–65
74. Smith MD, Karunadasa HI. 2018. White-light emission from layered halide perovskites. *Acc. Chem. Res.* 51(3):619–27
75. Song KS, Williams RT, eds. 1993. *Self-Trapped Excitons*. Springer Ser. Solid-State Sci., Vol. 105. Berlin, Heidelberg: Springer-Verlag
76. Kahmann S, Tekelenburg EK, Duim H, Kamminga ME, Loi MA. 2020. Extrinsic nature of the broad photoluminescence in lead iodide-based Ruddlesden-Popper perovskites. *Nat. Commun.* 11:2344
77. Wang X, Meng W, Liao W, Wang J, Xiong R-G, Yan Y. 2019. Atomistic mechanism of broadband emission in metal halide perovskites. *J. Phys. Chem. Lett.* 10(3):501–6
78. Ravindra NM, Auluck S, Srivastava VK. 1979. Temperature dependence of the energy gap in PbS, PbSe, and PbTe. *Phys. Status Solidi* 52(2):K151–55
79. Singh S, Li C, Panzer F, Narasimhan KL, Graeser A, et al. 2016. Effect of thermal and structural disorder on the electronic structure of hybrid perovskite semiconductor $CH_3NH_3PbI_3$. *J. Phys. Chem. Lett.* 7(15):3014–21
80. Trots DM, Myagkota SV. 2008. High-temperature structural evolution of caesium and rubidium triiodoplumbates. *J. Phys. Chem. Solids* 69(10):2520–26
81. Chemla D, Miller D, Smith P, Gossard A, Wiegmann W. 1984. Room temperature excitonic nonlinear absorption and refraction in GaAs/AlGaAs multiple quantum well structures. *IEEE J. Quantum Electron.* 20(3):265–75
82. Wright AD, Verdi C, Milot RL, Eperon GE, Pérez-Osorio MA, et al. 2016. Electron-phonon coupling in hybrid lead halide perovskites. *Nat. Commun.* 7:11755
83. Neutzner S, Thouin F, Cortecchia D, Petrozza A, Silva C, Srimath Kandada AR. 2018. Exciton-polaron spectral structures in two-dimensional hybrid lead-halide perovskites. *Phys. Rev. Mater.* 2(6):064605
84. Dammak T, Koubaa M, Boukheddaden K, Bougzhala H, Mlayah A, Abid Y. 2009. Two-dimensional excitons and photoluminescence properties of the organic/inorganic $(4\text{-}FC_6H_4C_2H_4NH_3)_2[PbI_4]$ nanomaterial. *J. Phys. Chem. C* 113(44):19305–9
85. Kaiser M, Li Y, Schwenzer J, Jakoby M, Allegro I, et al. 2021. How free exciton-exciton annihilation lets bound exciton emission dominate the photoluminescence of 2D-perovskites under high-fluence pulsed excitation at cryogenic temperatures. *J. Appl. Phys.* 129(12):123101
86. Gauthron K, Lauret J-S, Doyennette L, Lanty G, Al Choueiry A, et al. 2010. Optical spectroscopy of two-dimensional layered $(C_6H_5C_2H_4\text{-}NH_3)_2\text{-}PbI_4$ perovskite. *Opt. Express* 18(6):5912
87. Demchenko AP, Tomin VI, Chou P-T. 2017. Breaking the Kasha rule for more efficient photochemistry. *Chem. Rev.* 117(21):13353–81

88. Fang H-H, Yang J, Adjokatse S, Tekelenburg E, Kamminga ME, et al. 2020. Band-edge exciton fine structure and exciton recombination dynamics in single crystals of layered hybrid perovskites. *Adv. Funct. Mater.* 30(6):1907979
89. Thouin F, Neutzner S, Cortecchia D, Dragomir VA, Soci C, et al. 2018. Stable biexcitons in two-dimensional metal-halide perovskites with strong dynamic lattice disorder. *Phys. Rev. Mater.* 2(3):034001
90. Thouin F, Srimath Kandada AR, Valverde-Chávez DA, Cortecchia D, Bargigia I, et al. 2019. Electron-phonon couplings inherent in polarons drive exciton dynamics in two-dimensional metal-halide perovskites. *Chem. Mater.* 31(17):7085–91
91. Tekelenburg EK, Kahmann S, Kamminga ME, Blake GR, Loi MA. 2021. Elucidating the structure and photophysics of layered perovskites through cation fluorination. *Adv. Opt. Mater.* 9(18):2001647
92. Urban JM, Chehade G, Dyksik M, Menahem M, Surrente A, et al. 2020. Revealing excitonic phonon coupling in $(PEA)_2(MA)_{n-1}Pb_nI_{3n+1}$ 2D layered perovskites. *J. Phys. Chem. Lett.* 11(15):5830–35
93. Srimath Kandada AR, Silva C. 2020. Exciton polarons in two-dimensional hybrid metal-halide perovskites. *J. Phys. Chem. Lett.* 11(9):3173–84
94. de Jong M, Seijo L, Meijerink A, Rabouw FT. 2015. Resolving the ambiguity in the relation between Stokes shift and Huang-Rhys parameter. *Phys. Chem. Chem. Phys.* 17(26):16959–69
95. Gaynor JD, Khalil M. 2017. Signatures of vibronic coupling in two-dimensional electronic-vibrational and vibrational-electronic spectroscopies. *J. Chem. Phys.* 147(9):094202
96. Guzelturk B, Winkler T, Van de Goor TWJ, Smith MD, Bourelle SA, et al. 2021. Visualization of dynamic polaronic strain fields in hybrid lead halide perovskites. *Nat. Mater.* 20(5):618–23
97. Wu X, Tan LZ, Shen X, Hu T, Miyata K, et al. 2017. Light-induced picosecond rotational disordering of the inorganic sublattice in hybrid perovskites. *Sci. Adv.* 3(7):sciadv.1602388
98. Thouin F, Valverde-Chávez DA, Quarti C, Cortecchia D, Bargigia I, et al. 2019. Phonon coherences reveal the polaronic character of excitons in two-dimensional lead halide perovskites. *Nat. Mater.* 18(4):349–56
99. Kagan CR, Mitzi DB, Dimitrakopoulos CD. 1999. Organic-inorganic hybrid materials as semiconducting channels in thin-film field-effect transistors. *Science* 286(5441):945–47
100. Blom PWM, Mihailetchi VD, Koster LJA, Markov DE. 2007. Device physics of polymer:fullerene bulk heterojunction solar cells. *Adv. Mater.* 19(12):1551–66
101. Hoppe H, Sariciftci NS. 2004. Organic solar cells: an overview. *J. Mater. Res.* 19(7):1924–45
102. Era M, Morimoto S, Tsutsui T, Saito S. 1994. Organic-inorganic heterostructure electroluminescent device using a layered perovskite semiconductor $(C_6H_5C_2H_4NH_3)_2PbI_4$. *Appl. Phys. Lett.* 65(6):676–78
103. Hattori T, Taira T, Era M, Tsutsui T, Saito S. 1996. Highly efficient electroluminescence from a heterostructure device combined with emissive layered-perovskite and an electron-transporting organic compound. *Chem. Phys. Lett.* 254(1–2):103–8
104. Dohner ER, Jaffe A, Bradshaw LR, Karunadasa HI. 2014. Intrinsic white-light emission from layered hybrid perovskites. *J. Am. Chem. Soc.* 136(38):13154–57
105. Wehrenfennig C, Liu M, Snaith HJ, Johnston MB, Herz LM. 2014. Homogeneous emission line broadening in the organo lead halide perovskite $CH_3NH_3PbI_{3-x}Cl_x$. *J. Phys. Chem. Lett.* 5(8):1300–6
106. Ishihara T, Hong X, Ding J, Nurmikko AV. 1992. Dielectric confinement effect for exciton and biexciton states in PbI_4-based two-dimensional semiconductor structures. *Surf. Sci.* 267(1–3):323–26
107. Mitzi DB, Chondroudis K, Kagan CR. 1999. Design, structure, and optical properties of organic–inorganic perovskites containing an oligothiophene chromophore. *Inorg. Chem.* 38(26):6246–56
108. Blancon J-C, Tsai H, Nie W, Stoumpos CC, Pedesseau L, et al. 2017. Extremely efficient internal exciton dissociation through edge states in layered 2D perovskites. *Science* 355(6331):1288–92
109. Zhu H, Miyata K, Fu Y, Wang J, Joshi PP, et al. 2016. Screening in crystalline liquids protects energetic carriers in hybrid perovskites. *Science* 353(6306):1409–13
110. Permogorov S. 1975. Hot excitons in semiconductors. *Phys. Status Solidi* 68(1):9–42
111. Singh J. 1994. Quantum-well perfection requirements for large-scale applications of exciton-base devices. *IEEE J. Quantum Electron.* 30(4):893–98

112. Wagner RW, Lindsey JS. 1994. A molecular photonic wire. *J. Am. Chem. Soc.* 116(21):9759–60
113. Lanty G, Bréhier A, Parashkov R, Lauret JS, Deleporte E. 2008. Strong exciton-photon coupling at room temperature in microcavities containing two-dimensional layered perovskite compounds. *New J. Phys.* 10(6):065007
114. Byrnes T, Kim NY, Yamamoto Y. 2014. Exciton-polariton condensates. *Nat. Phys.* 10(11):803–13